Environmental Science & Technology

pubs.acs.org/est

Article

Quantitative Benchmarking of Catalytic Parameters for Enzyme-Mimetic Ribonucleotide Dephosphorylation by Iron Oxide Minerals

Jade J. Basinski, Sharon E. Bone, Aurore Niyitanga Manzi, Nasrin Naderi Beni, Fernando R. Tobias, Marcos Sanchez, Cynthia X. Cheng, Wiriya Thongsomboon, and Ludmilla Aristilde*

Cite This: *Environ. Sci. Technol.* 2025, 59, 5568−5584

Read Online

ACCESS | Metrics & More | Article Recommendations | Supporting Information

ABSTRACT: Iron oxides, which are documented phosphorus (P) sinks as adsorbents, have been shown to catalyze organic P dephosphorylation, implicating these minerals as catalytic traps in P cycling. However, quantitative evaluation of this abiotic catalysis is lacking. Here, we investigated the dephosphorylation kinetics of eight ribonucleotides, with different nucleobase structures and P stoichiometry, reacting with common iron oxides. X-ray absorption spectroscopy determined that 0−98% of mineral-bound P was recycled inorganic P (P_i). Matrix-assisted laser desorption/ionization with mass spectrometry demonstrated short-lived triphosphorylated and monophosphorylated ribonucleotides bound to goethite. Based on Michaelis-Menten type modeling of the kinetic evolution of both dissolved and mineral-bound P_i, maximal P_i production rates from triphosphorylated ribonucleotides reacted with goethite (1.9−16.1 μmol P_i h^{-1} $g_{goethite}^{-1}$) were >5-fold higher than with hematite and ferrihydrite; monophosphorylated ribonucleotides generated only mineral-bound P_i at similar rates (0.0−12.9 μmol P_i h^{-1} $g_{mineral}^{-1}$) across minerals. No clear distinction was observed between purine-based and pyrimidine-based ribonucleotides. After normalization to mineral-dependent P_i binding capacity, resulting catalytic turnover rates implied surface chemistry-controlled reactivity. Ribonucleotide−mineral complexation mechanisms were identified with infrared spectroscopy and molecular modeling. We estimated iron oxide-catalyzed rates in soil (0.01−5.5 μmol P_i h^{-1} g_{soil}) comparable to reported soil phosphatase rates, highlighting both minerals and enzymes as relevant catalysts in P cycling.

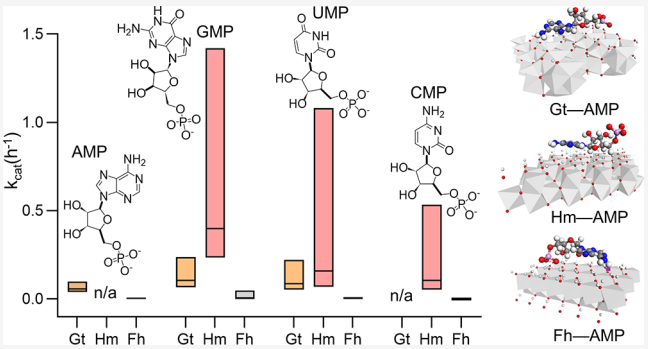

KEYWORDS: *kinetic parameters, ribonucleotide, iron oxide, goethite, hematite, ferrihydrite, phosphorus cycle*

1. INTRODUCTION

Biogeochemical cycling of phosphorus (P) plays a critical role in P availability in soils, fertilization of lakes and oceans, and agricultural productivity for food security. Iron (Fe) oxyhydroxides and oxides, collectively called Fe oxides here, are naturally occurring minerals that have been well documented to control the chemical and biological fates of P.[1−6] These minerals, which can be found at concentrations of up to 200 g Fe kg^{-1} dry weight in soils and sediments,[7−9] are reported to sequester up to 50% of the total soil P.[2−5] Due to their prevalence and strong adsorption capacity, Fe oxides are thus considered to serve as P sinks[5] in natural environments. Importantly, Fe oxides are also reported to catalyze the transformation of the less bioavailable organic P (P_{org}) to produce the readily bioavailable inorganic P (P_i), leading to the proposal of an additional role of Fe oxides in the P cycle as a source of bioavailable P.[10] Given that P_{org} can account for 20−60% of the total P content in soils[11] and sediments,[12] understanding the coupled adsorption and catalytic reactivities of Fe oxides[13−17] toward P_{org} is critical in evaluating the contribution of Fe oxides to the biogeochemical cycling of P. Common Fe oxides include those in crystalline phases such as goethite and hematite, as well as semicrystalline phases such as ferrihydrite.[18] With a high surface area (~200 m^2 g^{-1}), ferrihydrite is known to undergo high P adsorption and is implicated in controlling P availability in soil and lake sediment,[5,13,19] particularly in regions with frequent redox cycling[5,20,21] or enriched in organic matter and microbial activity.[9,22,23] Goethite and hematite, which have relatively low surface area (~30 m^2 g^{-1}), are two thermodynamically stable Fe oxides that are ubiquitous in the natural environment.[13,18,24] Here, we investigated the kinetics of these three common Fe oxides in catalyzing the dephosphorylation of different ribonucleotide structures to capture the effects of

Received: November 6, 2024
Revised: February 5, 2025
Accepted: February 6, 2025
Published: March 4, 2025

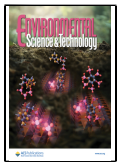

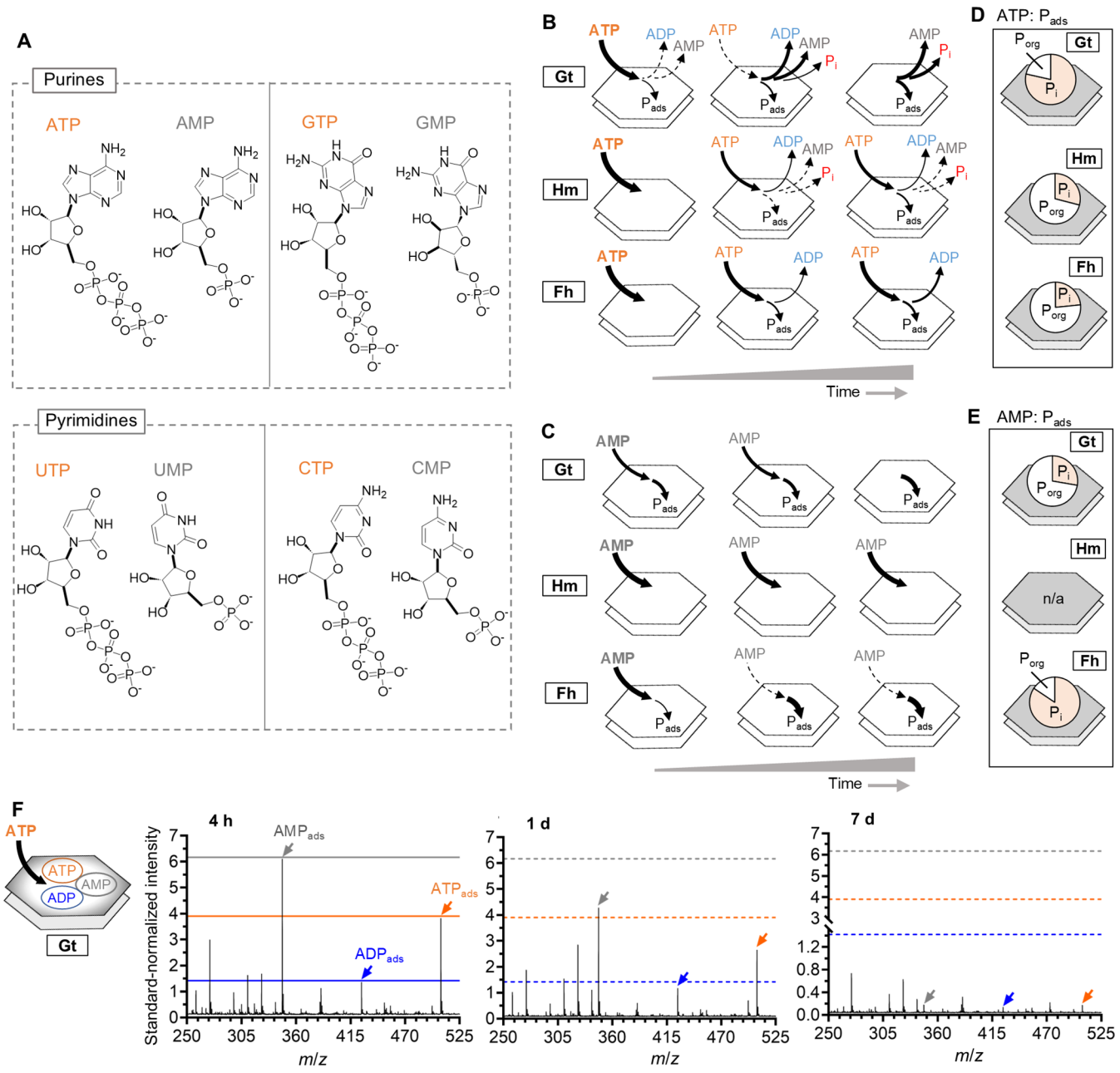

Figure 1. Evolution of ribonucleotide dephosphorylation templated on Fe oxide surfaces. (A) Chemical structures of (top) purine-based and (bottom) pyrimidine-based ribonucleotide structures investigated in this study: ATP, AMP, GTP, GMP, UTP, UMP, CTP, and CMP. Schematic illustration of reported[14,14] time-dependent transformation during the 7-d reaction of (B) ATP and (C) AMP with (top) goethite (Gt), (middle) hematite (Hm), and (bottom) ferrihydrite (Fh) based on solution analysis by UV-vis spectroscopy for inorganic P (P_i) and high-resolution LC-MS for the P_{org} reactant and products. Reported P_i and P_{org} fractions of total adsorbed P (P_{ads}) after 7-d reactions of (D) ATP and (E) AMP reactions with (top) Gt, (middle) Hm, and (bottom) Fh based on the analysis of particulate species by P K-edge XANES spectroscopy. (F) Dynamic changes in adsorbed levels of ATP, ADP, and AMP on the goethite surface monitored by MALDI-MS during the ATP reaction with goethite after 4 h (left), 1 d (middle), and 7 d (right). In (E), Pads was not available (n/a) for AMP reaction to hematite.

different functional groups in P_{org} and Fe oxide type on reactivity (Figure 1A).

Most prior studies on Fe oxide-mediated P_{org} transformation have focused on products found in solution. By applying ultraviolet−visible (UV−vis) spectroscopy to analyze P_i in solution, goethite,[13,15] hematite,[13,15] and an amorphous Fe oxide[13] were found to dephosphorylate *para*-nitrophenyl phosphate (*p*NPP), a synthetic P_{org} compound used widely as a model P_{org} in research investigations. Production of P_i in solution was also observed with naturally occurring P_{org} compounds such as adenosine triphosphate (ATP), adenosine monophosphate (AMP), glycerol phosphate, and glucose-6-phosphate.[10,16] In addition to dissolved P_i, liquid chromatography−mass spectrometry (LC-MS) has been applied to monitor organic dephosphorylation products of ATP after reactions with goethite, hematite, and ferrihydrite.[10,14,17] The LC-MS data revealed step-by-step sequential dephosphorylation of ATP to ADP and AMP by the minerals[10,14,17] (Figure 1B), as has been demonstrated with phosphatase-like enzymes.[25] Subsequent mass balance analysis determined

https://doi.org/10.1021/acs.est.4c12049
Environ. Sci. Technol. 2025, 59, 5568−5584

that a fraction of the generated P_i from the ATP dephosphorylation was missing from solution and instead remained adsorbed on the mineral surface.[10,14,17] Interestingly, when the LC-MS analysis was performed after AMP reactions with the same three Fe oxide minerals, no dephosphorylated product was measured in solution, but there was clear evidence of AMP adsorption in the case of ferrihydrite and goethite (Figure 1C). As a surface-based technique, P K-edge X-ray absorption near-edge structure (XANES) spectroscopy has afforded direct quantification of the relative fractions of P_i versus P_{org} adsorbed on the Fe oxides (Figure 1D,E).[26] For instance, while mass balance analysis based on inorganic and organic species of P in solution has determined that ∼12% of ferrihydrite-bound P derived from ATP was adsorbed P_i, the XANES data revealed that this was an underestimation and, instead, there was 3-fold higher amount of P_i trapped on this Fe oxide surface[14] (Figure 1D). With regard to the adsorbed P from the AMP reactions, up to 87% was determined remarkably to be adsorbed P_i on ferrihydrite and goethite;[14] this observation was made possible only by applying the XANES analysis due to the absence of both P_i and dephosphorylated products in solution (Figure 1E). Therefore, direct surface characterization of P speciation is necessary to understand the catalytic reactivity of Fe oxides. Still, the XANES technique is not able to identify the different types of P_{org} compounds within the adsorbed P_{org} fraction on the Fe oxide surface.[10] The application of matrix-assisted laser desorption/ionization (MALDI) MS may provide a useful approach to overcome this analytical limitation.[27] For instance, with MALDI combined with time-of-flight MS, dephosphorylated organic products could be distinguished from the P_{org} reactant, to facilitate direct monitoring P_{org} transformation on an Fe oxide surface.[27]

Varying extents of dephosphorylation reactivity of Fe oxides have been reported for different P_{org} compounds.[10,13−17] Baldwin et al.[13] reported the following decreasing order for the initial hydrolysis rates of *p*NPP (starting concentration of 15 μM *p*NPP-P): 18.0 μM P h^{-1} $g_{mineral}^{-1}$ with an amorphous Fe oxide, 8.6 μM P h^{-1} $g_{mineral}^{-1}$ with hematite, and 4.5 μM P h^{-1} $g_{mineral}^{-1}$ with goethite. Apparent maximum rates of dephosphorylation (V_{max}) of a natural P_{org}, which have been determined only for ATP after kinetics experiments at varying ATP concentrations, indicated that goethite was the most reactive with a V_{max} of 3.2−6.4 μM P h^{-1}, 7-fold higher than hematite (0.2−0.7 μM P h^{-1}) and 2-fold higher than ferrihydrite (2.6−4.2 μM P h^{-1}).[10] The maximal catalytic rates for AMP, other ribonucleotides, and other P_{org} compounds remain to be determined.

Mineral-dependent specific surface area was proposed previously as a controlling factor in the efficiency of heterogeneous catalysts.[28] However, surface area alone could not account for the differences in P_{org} dephosphorylation by Fe oxides.[10,13,17] For instance, greater than 16-fold more P_i was generated from goethite-catalyzed dephosphorylation of ATP compared to ferrihydrite, despite a 10-fold greater surface area of ferrihydrite than goethite.[10] Therefore, the surface chemistry of the Fe oxide and the conformation of the adsorbed P_{org} are both worthy of consideration to gain insights on Fe oxide-catalyzed transformation of different P_{org} compounds.

Both experimental studies and molecular modeling simulations have been used to investigate the binding of P_i,[29−35] nucleic acids (DNA,[4,36,37] RNA[14]), ribonucleotides (ATP,[4,14,36] ADP,[14,36] and AMP[4,14,14]), phytate,[31] glycerol phosphate,[31] trimethyl phosphate,[34] and triethyl phosphate[34] on Fe oxides. Hydroxyl groups on the mineral surface[38−40] are well acknowledged to drive the adsorption of P_i by mediating inner sphere complexes through ligand exchange with coordinated hydroxyls on the Fe oxide surface.[4,33,36,39,41] Attenuated total reflectance-Fourier-transform infrared (ATR-FTIR) spectroscopy has been used to probe different binding modes of P_i onto the Fe oxide surface: monodentate (binding interaction at one site on the adsorbent), mononuclear bidentate (binding interaction of one adsorptive atom at two sites on the adsorbent), and binuclear bidentate (binding interactions at two different sites on the adsorbent through two separate atoms of the adsorptive).[29−33,42] Experimental and simulated FTIR spectra generated from molecular models of bound P_i have revealed monodentate and bidentate binding in both mononuclear and binuclear complexes.[29,31,33] While the adsorption mechanisms of P_i onto Fe oxides have been well studied, the corresponding mechanisms for the adsorption of environmentally relevant P_{org} compounds remain largely unknown.

Understanding P_{org} binding and the resulting catalytic activity of Fe oxides is further complicated by the diversity of the chemical structures in P_{org} compounds. Relevant P_{org} biomolecules include high-molecular-weight nucleic acid polymers (DNA and RNA), (deoxy)-ribonucleotide monomers, sugar phosphates (e.g., glucose-6-phosphate), phytate, phospholipids, and phosphonates (e.g., 2-aminoethylphosphonate). These different types of P_{org} compounds exhibit a variety of P bonds: phosphoester (C−O−P), phosphoanhydride (P−O−P), and phosphonate (C−P).[43−46] Therefore, due to the chemical complexity of P_{org} compounds, various binding modes of P_{org} compounds onto Fe oxides have been reported. For instance, on goethite, molecular modeling of stable conformations indicated that binding of glycerol phosphate was mediated through the phosphate moiety by both monodentate and bidentate modes,[31] while binding of phytate involved one to three mononuclear monodentate interactions.[31] Like P_i adsorption onto Fe oxides, ATR-FTIR bands of DNA adsorption onto goethite highlighted mononuclear monodentate binding through the phosphate moiety as the dominant adsorption mechanism.[36,37] However, the simulated adsorption of ribonucleotides on ferrihydrite revealed multiple mononuclear monodentate modes mediated through both the phosphate group and organic moieties.[14] Experimental data have revealed the adsorption capacity of goethite was dependent on the identity of the nucleobase,[36] with the following increasing order in the adsorption of ribonucleotides with different nucleobases: uracil < thymine < cytidine ≈ adenine < guanine.[36] These results implied that non-P-containing moieties of P_{org} such as contributions from the electron density of π bonds in the nucleobase would influence adsorption onto Fe oxides,[36] albeit the underlying adsorption mechanism has not yet been elucidated. As adsorption is the first step in catalysis, differences in P_{org} binding conformations are proposed to dictate the catalytic reactivity[10,14,16,17,47] exhibited by Fe oxides for different P_{org} compounds.

Here, we investigated the adsorption and catalytic reactivities of three common Fe oxides (goethite, hematite, and ferrihydrite) toward eight structurally different ribonucleotides. We considered both monophosphorylated and triphosphorylated ribonucleotides with purine bases (adenine or guanine) or pyrimidine bases (cytosine or uracil) to capture the reactivity toward phosphoester versus phosphoanhydride

https://doi.org/10.1021/acs.est.4c12049
Environ. Sci. Technol. 2025, 59, 5568−5584

bonds in P_{org} compounds with different organic moieties (Figure 1A). We obtained P K-edge XANES data to determine the relative fractions of P_i and P_{org} bound to the Fe oxide surface after reactions with each ribonucleotide reactant. To monitor the evolution of different P_{org} species adsorbed on a mineral surface, we employed MALDI coupled to MS. We performed molecular modeling simulations to obtain optimized adsorbate conformations with predicted binding interactions. From ATR-FTIR spectroscopic analysis of the ribonucleotide−mineral complexes after adsorption experiments, we identified the different moieties of the ribonucleotide structures involved in binding with the Fe oxide surfaces. We conducted Michaelis−Menten-type kinetics analysis to determine the V_{max} and turnover rate (k_{cat}) parameters for the dephosphorylation of the suite of ribonucleotides with the different Fe oxides. The present study provides the first report of detailed kinetics of Fe oxide-catalyzed P_{org} dephosphorylation for a complete range of ribonucleotide structures, comprising four nucleobases (adenine, guanine, cytosine, or uracil) in RNA and two phosphorylation states (monophosphorylated or triphosphorylated). Finally, we employed our kinetic parameters to obtain estimated Fe oxide-catalyzed rates at different Fe oxide content in soils and compare these abiotic rates with reported phosphatase-type enzymatic rates in soils. Taken together, the new insights provided by our data advance quantitative understanding of both Fe oxide-specific and functional group-specific factors that dictate the reactivity of Fe oxides toward P_{org} dephosphorylation.

2. MATERIALS AND METHODS

2.1. Chemicals. Details on the ribonucleotide reactants and products purchased for this study are listed in Table S1. Briefly, these compounds are ATP, ADP, AMP, adenosine, adenine, guanosine triphosphate (GTP), guanosine diphosphate (GDP), guanosine monophosphate (GMP), guanosine, guanine, uridine triphosphate (UTP), uridine diphosphate (UDP), uridine monophosphate (UMP), uridine, uracil, cytidine triphosphate (CTP), cytidine diphosphate (CDP), cytidine monophosphate (CMP), cytidine, cytosine, and P_i as sodium phosphate. Goethite and hematite were purchased from Alfa Aesar and Strem Chemicals, respectively; ferrihydrite was synthesized using the methodology by Schwertmann and Cornell[48] and confirmed to be 2-line ferrihydrite by X-ray diffraction data as reported previously.[10] The identity of the other minerals were also confirmed by X-ray diffraction. All solutions were prepared with purified water using a GenPure system (Thermo Scientific; 18.2 MΩ cm).

2.2. Kinetic Dephosphorylation Reactions of Ribonucleotide Compounds with Fe Oxides. Triplicate experiments were conducted for reactions of each Fe oxide (goethite, hematite, and ferrihydrite; 1 g L^{-1}) with each ribonucleotide reactant (ATP, AMP, GTP, GMP, UTP, UMP, CTP, and CMP) over a range of concentrations (20 μM, 25 μM, 50 μM, 125 μM, 200 μM, and 400 μM) and reaction times (2, 4, 8, 12, 16, 24, and 48 h). Reactions were initiated by adding 40 mL of reactant solution consisting of 0.1 M $NaNO_3$ and 0.01 M $NaHCO_3$ (adjusted to pH = 7.0 using 2 M HNO_3) with the specific ribonucleotide concentration to 50 mL polypropylene tubes containing Fe oxide. Reactions were performed in the absence of light and shaken at 150 rpm in an incubator shaker (Eppendorf Innova S44i) at 298 K. To stop the reactions at each time point, the Fe oxide particles were removed from the reaction solution by filtration through a 0.2-μm filter. Aliquots of the filtrate were used for the analysis of P_i and P_{org} in solution. The filtrate was frozen at −20 °C until analysis of organic species by high-resolution LC-MS.

2.3. Analysis of Reactants and Products in Solution. The concentration of P_i in solution was quantified by a colorimetric phosphomolybdate method using a Cary 60 UV−visible spectrophotometer.[49] The organic compounds (the ribonucleotide reactants and their corresponding products) in solution were quantified using our previously established LC-MS method.[14] The specific compounds analyzed were ATP, ADP, AMP, adenosine, adenine, GTP, GDP, GMP, guanosine, guanine, UTP, UDP, UMP, uridine, uracil, CTP, CDP, CMP, cytidine, and cytosine. The LC-MS system consisted of a Dionex Ultimate 3000 LC instrument coupled to a Q-Exactive mass spectrometer. Measurements and analyses were collected and performed using the Xcalibur software (Thermo Scientific). The compounds were separated by a Waters Acquity UPLC BEH C18 column (2.1 mm × 100 mm × 1.7 μm) using a 25 min gradient of solvent A (3% v/v methanol/15 mM acetic acid/10 mM tributylamine) and solvent B (100% methanol). The mass spectrometer was run in negative ion mode at an MS range of mass-overcharge (m/z) 100 to 600 with a resolution of 70,000. Standard solutions of the compounds, ranging from 0.5 to 15 μM, were used for calibration. Samples with concentrations of above 15 μM were diluted to obtain accurate quantification data within the calibration range. All compounds were quantified using the peak area integrated across the elution time of the ion chromatograms in the specific m/z channel for each compound. Quality controls were run every 9 to 12 samples and remained within 30% error. Beyond this error in the LC-MS signal intensity in quality controls, concentrations of P_{org} compounds were adjusted accordingly.

Before employing XANES to account for the partitioning of P_{org} and P_i in the adsorbed P ($P_{adsorbed}$) on the Fe oxide surfaces, we used mass balance based on the concentration of species in solution to determine $P_{adsorbed}$ at each time point using the following equations:

$$P_{total}(t) = P_{initial} \quad (1)$$

$$P_{total}(t) = P_{solution}(t) + P_{adsorbed}(t) \quad (2)$$

$$P_{solution}(t) = P_{i,solution}(t) + P_{org,solution}(t) \quad (3)$$

$$P_{adsorbed}(t) = P_{initial} - P_{i,solution}(t) - P_{org,solution}(t) \quad (4)$$

$$P_{org,solution}(t) = 3 \times XTP_{solution} + 2 \times XDP_{solution} + XMP_{solution} \quad (5)$$

$$P_{adsorbed}(t) = P_{initial} - P_{i,solution} - 3 \times XTP_{solution} - 2 \times XDP_{solution} - XMP_{solution} \quad (6)$$

where XTP, XDP, and XMP represent the concentration of triphosphorylated, dephosphorylated, and monophosphorylated ribonucleotide compounds, respectively. To test the reliability of our analytical quantitation, we compared the initial P ($P_{initial}$) added to the total amount (P_{total}) measured in solution for the control samples without minerals as a function of time. For the samples with a triphosphorylated ribonucleotide (i.e., XTP = ATP, GTP, or UTP) as the reactant, over 90% of the controls had P_{total} values within 20% of the

https://doi.org/10.1021/acs.est.4c12049
Environ. Sci. Technol. 2025, 59, 5568−5584

expected value. For the samples with a monophosphorylated ribonucleotide (i.e., XMP = AMT, GMP, or UMP) as the reactant, about half of the samples did not have a P_{total} value in solution within 20% of $P_{initial}$ due to the loss of sensitivity of the LC-MS instrument. Quality control tests revealed that when a decrease in sensitivity occurred, it was the same across all samples processed in the same batch in the instrument. Therefore, we were able to use our control samples to correct for this sensitivity issue.

2.4. Probing Surface-Localized Ribonucleotides by MALDI-MS. To understand the speciation of ribonucleotide reactant and product bound to the Fe oxide surface throughout the reaction, we performed MALDI-MS. Incubations of goethite and ATP were chosen for this analysis due to the reported high reactivity of goethite with ATP.[10,17] Similar to the protocol described above for the kinetic dephosphorylation reactions, reactions for MALDI-MS analysis were prepared with 40 mL of reaction solution containing 250 μM of ATP with 1 g L^{-1} of goethite and shaken for 4 h, 1 day, or 7 days at 150 rpm in the absence of light. Reactions were stopped by vacuum filtration to collect all the reacted goethite particles on a filter and rinsed with purified water. Following the freeze-drying of the mineral particles removed from the filters, a 200-μL suspension of the dried particles was prepared with 500 μM of glucose-6-phosphate to be used as an internal standard in the MALDI-MS analysis. A 1:1 v:v mixture of the suspension (10 μL) and a matrix (10 μL) (composed of 15 g L^{-1} of 9-aminoacridine in a solvent mixture of 75% acetonitrile and 25%) was mixed vigorously (1 min) followed by deposition of a 2-μL aliquot of the mixture on a MALDI plate and left to dry before analysis.

Mass spectra were obtained using a Bruker rapifleX TissueTyper MALDI coupled with a time-of-flight mass spectrometer equipped with a 3D smart beam laser system for enhanced spatial resolution, collected by the FlexControl data acquisition software, and processed using FlexAnalysis software for data analysis. All spectra were obtained in negative ion reflector mode across the 10−4000 mass-to-charge ratio (m/z) range, averaging 2000−4000 laser shots. Laser beam attenuation was set between 41 and 50% at a 10 kHz repetition rate. Initial mass calibration was performed using red phosphorus, and calibration was maintained throughout the experiment.

2.5. P K-Edge XANES Spectroscopy and Analysis of Adsorbed P_i and P_{org} Speciation. Samples for XANES analysis of Fe oxide samples with reacted ribonucleotide were prepared by adding 400 mL of the aforementioned reaction solution with 50 μM ribonucleotide in a 500 mL polypropylene bottle with 1 g L^{-1} of Fe oxide. The samples were reacted for 75 min or 7 d before stopping the reaction by vacuum filtration, followed by rinsing the filters containing the mineral particles with a small volume (~5 mL) of purified water. The collected particles were freeze-dried and ground before XANES analysis. The rinsing step is important to remove residual background salts and loosely bound P reactants, which may crystallize after the drying procedure and thus interfere with the subsequent XANES analysis. We note that the rinsing step would not underestimate the total adsorbed P, which was determined independently based on the mass balance on the solution species (eq 4).

The P K-edge XANES spectroscopy was conducted at the Stanford Synchrotron Radiation Lightsource (SSRL) on the 14-3 beamline. The ground samples were applied in a thin layer to Mylar tape and then affixed to a sample holder for analysis. The spectra were collected at room temperature in fluorescence mode with a Vortex detector under a helium atmosphere with vertical slits set to 1 mm and horizontal slits set to 2.5 mm. The energy was selected using a Si(111) monochromator and calibrated to the energy of the first pre-edge feature of PPh_4-Br (2146.96 eV). All collected spectra were normalized before being used in a linear combination fitting analysis. All data processing was performed in the Athena module of the IFEFFIT software package.[50] The normalization process consisted of fitting a line to the pre-edge region (−24.5 to −14.5 eV) of the spectrum and fitting a second-order polynomial to the postedge region (15.0 to 85.0 eV). The pre-edge line was subtracted from the spectrum to remove the background signal, and the absorption jump at the first inflection point was set to an intensity of 1.0 based on the difference between the pre- and postedge fits. For linear combination fitting, the spectra of the endmember samples with Fe oxides (using 75-min reaction with each ribonucleotide and the published spectra for 7-d reaction with P_i[10]) were combined to generate a combined spectrum fitted to that of the 7-d reacted sample. Fits were considered acceptable when three criteria were met: matching of the rising edge, white line peak shape, and postedge region shape; the sum of all components was between 0.90 and 1.10, and the R-factor was less than 0.10.

2.6. Solid-State ATR-FTIR Spectroscopy. For collection of the ATR-FTIR spectra, separate adsorption experiments were conducted with ATP, AMP, P_i (as sodium phosphate), and adenine with the Fe oxides. Goethite, hematite, and ferrihydrite (1 g L^{-1}) were reacted with the different reactants (ATP, AMP, adenine, and P_i) at two concentrations (50 or 200 μM) in a 50-mL polypropylene centrifuge tube with 40 mL of reaction solution shaken for 7 days at 150 rpm in an incubator shaker. These adsorption reactions for the ATR-FTIR analysis were prepared using a background solution with only 0.1 M NaCl solution (adjusted to pH 7.0) to avoid the interference of $NaNO_3$ and $NaHCO_3$ with the spectral features of interest. These adsorption reactions were stopped using vacuum filtration through a 0.2 μm filter to collect the reacted mineral particles, which were rinsed with purified water (~5 mL), freeze-dried, and then ground before ATR-FTIR measurements.

The ATR-FTIR spectra were collected using a Bruker Vertex 70 FTIR spectrophotometer with a mid-infrared light source, room-temperature DLaTGS detector, KBr beamsplitter and optic windows, and OPUS 7.2 software (Bruker). Before each sample, a background spectrum of ambient air with the pressure clamp lowered was recorded using the same parameters as sample spectra collection: collection from 4000 to 600 cm^{-1} at a resolution of 4 cm^{-1} and 128 coadded scans using the MIRacle ATR stage (PIKE) with a diamond crystal and a pressure clamp. After background collection, a small amount of the dried ground samples was placed on the MIR crystal, and the pressure clamp was lowered. Data analysis was performed by using the OPUS software. For each sample, the spectrum range was set as 1800 cm^{-1} to 750 cm^{-1}, and a rubber-band baseline correction (64 points) was applied.

2.7. Molecular Simulations of Adsorbate Conformations. Molecular modeling simulations of a set of triphosphorylated and monophosphorylated ribonucleotides (ATP and AMP, respectively) adsorbed onto the Fe oxides were performed using BIOVIA's Materials Studio software pack-

https://doi.org/10.1021/acs.est.4c12049
Environ. Sci. Technol. 2025, 59, 5568−5584

age.[51] The Fe oxide structures were prepared in accordance with published crystal data for goethite,[52] hematite,[53] and ferrihydrite[54,55] to obtain mineral structures with the following lattice parameters: average stoichiometries of FeO_2H (39.8 Å × 36.8 Å × 54.5 Å) for goethite, $FeO_{1.875}H_{0.75}$ (40.3 Å × 40.3 Å × 61.2 Å) for hematite, and $FeO_{2.5}H_{2.12}$ (41.2 Å × 42.2 Å × 61.0 Å) for ferrihydrite. The atomic charges of the Fe oxide lattices were assigned based on the CLAYFF force field designed for the modeling of mineral oxide structures.[56] Optimized ribonucleotide reactant structures were generated using geometry optimization calculated using density function theory with the Becke, 3-parameter, Lee−Yang−Parr (B3LYP) hybrid density functional.[57] Partial charges were calculated using the Hirshfeld method[58] for further simulation work. We ran a 10 ns molecular dynamics equilibration of the fully hydrated ribonucleotide structures with explicit water molecules described by the extended simple point charge water model (SPC/E).[59] Molecular interactions were simulated using the condensed-phase optimized molecular potentials for atomistic simulation studies (COMPASS) force field (version III).[60] The parametrization of the optimized ribonucleotide structures was validated by comparison of our simulated ATP structure to reported X-ray crystallography data.[61,62] Specifically, our optimized ATP structure had bond lengths and bond angles with 100% agreement (within an imprecision of two standard deviations) and 60% agreement (within an imprecision of two standard deviations), respectively, to the reported X-ray crystallography data[61,62] (Tables S2−S4). After this validation with ATP, the same protocol was performed to generate an optimized AMP structure (Tables S5−S7). For the subsequent adsorption simulations performed with dry systems, the optimized ribonucleotide structures were removed from their hydration boxes to be in accordance with the ATR-FTIR data obtained under dry conditions.

For the preparation of the periodic ribonucleotide−mineral system, a vacuum slab of 50 Å thickness was placed above the mineral surfaces to provide adequate space for the adsorptives (ribonucleotide, Na^+, and Cl^-) and thus avoid the effects of periodic reflections. The ribonucleotide structures were adsorbed on the mineral surface using the Adsorption Locator module of Materials Studio. Specifically, we implemented a Monte Carlo approach that consisted of translation and rotational steps over a temperature cycle of 298 to 600 K to determine the most energetically favorable adsorbate conformation. After the most energetically favorable conformation was obtained, we surveyed the formation of hydrogen bonds (H-bonds) between the ribonucleotide and the mineral surface using 2.5 Å as the maximum H-bond distance and 120° for the minimum H-bond-donor−acceptor angle.

2.8. Modeling Catalytic Parameters of the Dephosphorylation Reaction Kinetics. The instantaneous rates of P_i generation (V) were determined from the initial slope from plotting the experimental data of the concentration of P_i generated as a function of time. This slope was calculated by regression analysis to obtain V at different concentrations (20 μM−400 μM) of each ribonucleotide reacted with each Fe oxide (1 g L^{-1}). For each set of reactions, we determined two V values: one for P_i in solution (directly determined by colorimetric analysis) and one for adsorbed P_i (determined by performing mass balance on P to obtain adsorbed P using eqs 1−6, followed by accounting for the P_i fraction in the adsorbed P through P-XANES analysis).

Michaelis−Menten-type kinetic modeling was performed to determine the kinetic parameters of the Fe oxide-catalyzed dephosphorylation reactions, based on the following equation:

$$V = \frac{V_{max} \times [R]}{K_m + [R]} \quad (7)$$

where V_{max} is the apparent maximal rate of reaction (achieved when the catalyst is fully saturated), [R] is the concentration of the ribonucleotide reactant, and K_m is the Michaelis constant or the concentration of the reactant required to achieve half of V_{max}.

To determine the V_{max} values, the collective V values for each set of ribonucleotide−mineral pairings were fitted to the Michaelis−Menten model within 95% confidence intervals using GraphPad (version 9.4.0). Subsequently, we calculated the turnover number or k_{cat}, which is a measure of the efficiency of each active site of the catalyst, using the following equation:

$$k_{cat} = \frac{V_{max}}{[E]} \quad (8)$$

where [E] typically denotes the enzyme concentration or active site concentration in the catalyst. Here, considering that Fe oxides are heterogeneous catalysts, we used the P_i binding site density of each Fe oxide as the "active site" concentration. The P_i binding site densities were reported previously.[10]

2.9. Statistical Analysis. Statistical significance for comparisons of kinetic parameters (V_{max} and k_{cat}) reported in the text or in the figures was calculated using the unpaired t test except with statistical significance determined by the F-test. The kinetic parameters for reactions of ATP only with the Fe oxides were from a data set published previously.[10] The error bars on P fractions obtained from LCF modeling of the XANES data represent the errors on the model fitting.

3. RESULTS AND DISCUSSION

3.1. Dynamic Evolution of Dephosphorylation Products on the Mineral Surface. As discussed above, previous kinetic dephosphorylation experiments with ATP and AMP,[10,14,17] which employed LC-MS analysis for the identification of dissolved organic species, revealed that the reactions of the three Fe oxides (i.e., goethite, hematite, and ferrihydrite) with monophosphorylated versus triphosphorylated adenine-based ribonucleotides resulted in different extents of produced P_i (Figure 1B,C). Importantly, application of XANES spectroscopy to determine surface speciation after 7-d reactions with ATP and AMP highlighted the presence of adsorbed P_i, which was not fully accounted for by performing mass balance based on solution data[10,17] (Figure 1D,E). The differences in the partitioning of adsorbed P_i versus adsorbed P_{org} after reactions of ATP and AMP implied different reactivities of monophosphorylated and triphosphorylated ribonucleotides with Fe oxides. Here, to investigate further the role of the reactant structures, we performed 7-d reactions of six additional ribonucleotides (GTP, GMP, UTP, UMP, CTP, and CMP) with the three Fe oxides and performed LC-MS and XANES analyses to determine the adsorption reactivity and fraction of adsorbed P_i versus adsorbed P_{org}.

First, from mass balance analysis on the solution species, we determined the amount of total P retained on the Fe oxide surfaces after reaction with the ribonucleotide reactants, with a 50 μM starting concentration (i.e., 150 μM P for the

https://doi.org/10.1021/acs.est.4c12049
Environ. Sci. Technol. 2025, 59, 5568−5584

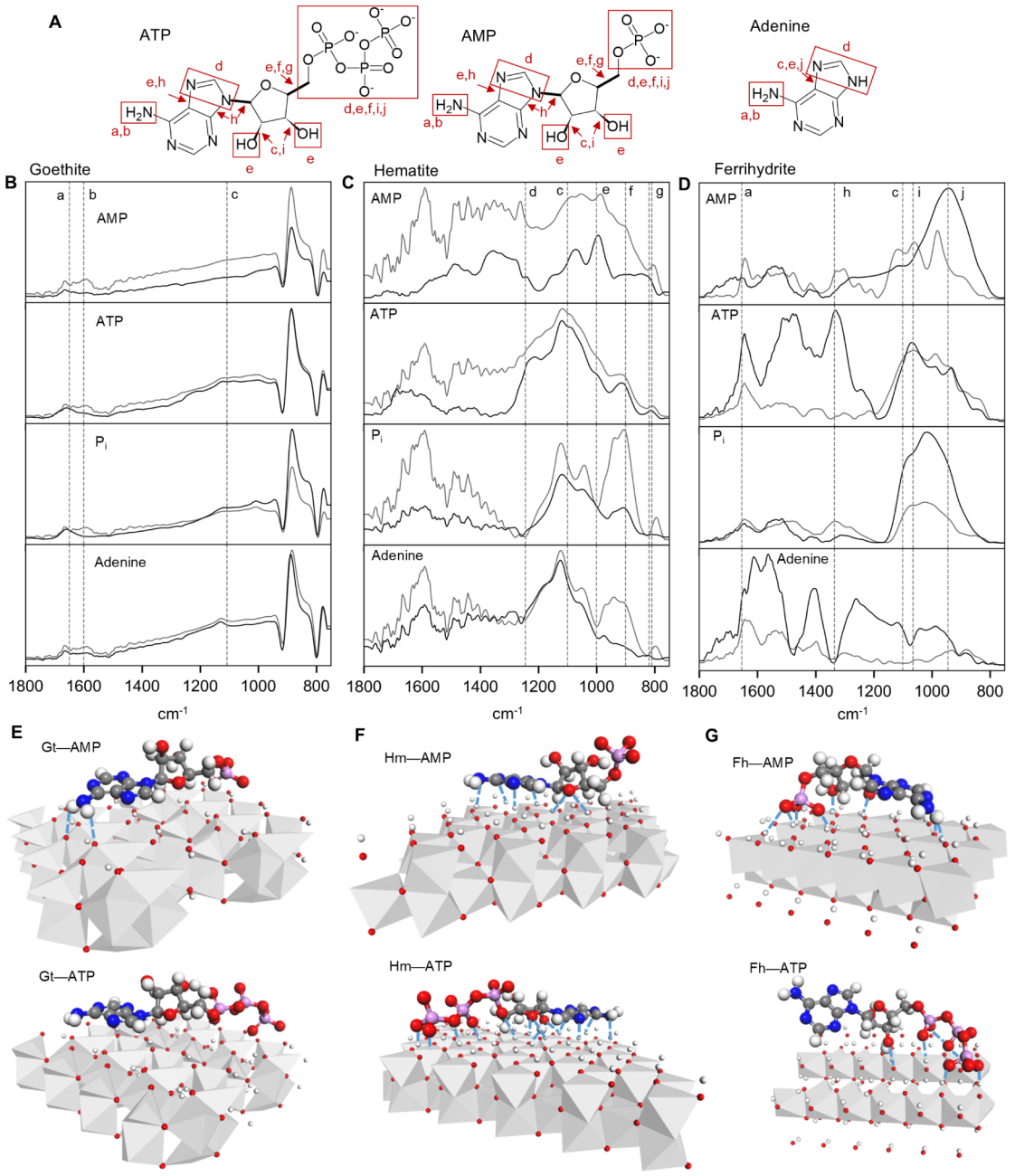

Figure 2. Adsorption Mmechanisms of ribonucleotides on iron oxide surfaces. (A) Vibration bands (indicated in letters and boxes) of bonds and moieties in ATP, AMP, and adenine identified by solid state FTIR spectroscopy after adsorption on Fe oxide surfaces. The ATR-FTIR spectra after adsorption of (from top to bottom) AMP, ATP, P_i, and adenine on (B) goethite, (C) hematite, and (D) ferrihydrite with the corresponding (E, F, G) energetically minimized adsorbate conformations of (top) AMP and (bottom) ATP. Relevant peaks in the ATR-FTIR spectra are shown by the dashed lines corresponding to the letters highlighted with the structures in panel A. In panels B–D, the two spectra shown represent reactions with 50 μM of the specified compound (light gray) and 200 μM of the specified compound (dark gray). In panels E–G, H-bonds predicted by molecular modeling simulations between the mineral surface and the adsorbed ribonucleotide are shown by dashed blue lines. Element key: Fe in light gray, H in white, oxygen in red, carbon in dark gray, nitrogen in blue, and phosphorus in pink.

triphosphorylated ribonucleotides and 50 μM P for the monophosphorylated ribonucleotides) (Table S8). With regard to adsorption reactivity for the different ribonucleotide structures, goethite and ferrihydrite adsorbed 3-fold to 6-fold more reactant-P from purine-based ribonucleotides (531–2013 μg P_{ads} $g_{mineral}^{-1}$) compared to pyrimidine-based ribonucleotides (45–639 μg P_{ads} $g_{mineral}^{-1}$; $p < 0.01$) (Table S8). Previous adsorption data of ribonucleotide reactions with goethite[36] and various manganese oxides[63] also reported higher adsorption with purine-based nucleotides than pyrimidine-based ribonucleotides, a difference that was attributed to the relatively higher amount of π electron density in the purine base compared to the pyrimidine base.[63] With hematite, which had a reportedly lower overall adsorption capacity of P_{org} compounds than ferrihydrite and goethite,[4] there was no statistical difference in adsorption of purines (25–1591 μg P_{ads} $g_{mineral}^{-1}$) versus adsorption of pyrimidines (32–384 μg P_{ads} $g_{mineral}^{-1}$) ($p = 0.19$) (Table S8). Thus, these data implied that both the reactant structure and Fe oxide type

https://doi.org/10.1021/acs.est.4c12049
Environ. Sci. Technol. 2025, 59, 5568–5584

influenced the total adsorption of P_{org} compounds onto Fe oxide surfaces.

We employed XANES spectroscopy to capture the extent to which the Fe oxide surfaces retained adsorbed P_{org} or adsorbed P_i. Due to low adsorbed P (less than 3% of initial reactant P), it was not possible to obtain P speciation (i.e., relative P_i and P_{org} fractions) on the mineral surface after reactions of AMP with hematite, CTP with goethite, and CTP with hematite (Table S8). The low adsorption of CTP by goethite was unexpected, but the low adsorption on hematite was expected because hematite was shown previously to exhibit 2-fold to 5-fold lower adsorption for P_{org} compounds than ferrihydrite and goethite.[10] With goethite, the triphosphorylated ribonucleotides (GTP, UTP) exhibited adsorbed P_i fractions (62%−67%) close to the fraction (78%) reported for ATP[10] (Figures 1D and S1A). Similarly, with hematite, the reaction with GTP and UTP resulted in an adsorbed P_i fraction (23%−32%) comparable to the fraction (29%) reported for ATP (Figures 1D and S1B). In contrast, while 23% adsorbed P_i fraction was reported[10] for ATP reacted with ferrihydrite, minimal adsorbed P_i (1%−7%) was obtained for the other triphosphorylated ribonucleotides (GTP, UTP, CTP) (Figures 1D and S1C). Interestingly, while reactions of CTP with goethite and hematite resulted in minimal P_i adsorption that was consistent with minimal P_{org} adsorption, the reaction of CTP with ferrihydrite resulted in minimal adsorbed P_i (1%) despite >6-fold more fraction of adsorbed CTP-derived P on ferrihydrite (Table S8 and Figure S1). These data with the triphosphorylated ribonucleotides highlighted the compound-dependent extent of adsorption and transformation of ribonucleotides by Fe oxides.

With respect to the monophosphorylated ribonucleotides, reactions of GMP and UMP with goethite resulted in a high fraction of adsorbed P (63% and 98%, respectively), while there was no adsorbed P_i detected with CMP and the reported adsorbed P_i fraction of AMP[14] was only 28% (Figures 1E and S1A). With hematite, while no adsorbed P was obtained after reaction with AMP[10] (Figure 1E), reactions of GMP, UMP, and CMP all resulted in P_i adsorbption on the surface (98%, 50%, and 66%, respectively) (Figure S1B). With ferrihydrite, the adsorbed P_i fraction after reactions with GMP, CMP, and UMP contained 4-fold to 10-fold lower fraction of adsorbed P_i (8% to 20%) than the reported value for AMP[10] (84%) (Figures 1E and S1B).

In sum, reactions of purine-based ribonucleotides with goethite and ferrihydrite resulted in 3-fold to 6-fold greater adsorbed P than pyrimidine-based ribonucleotides ($p < 0.01$). In the case of goethite, this difference translated to a 5-fold higher adsorbed P_i fraction from the purine-based ribonucleotides ($p < 0.05$). In contrast, the adsorbed P_i fractions derived from purine-based and pyrimidine-based ribonucleotides adsorbed to ferrihydrite were comparable ($p = 0.11$) (Table S11 and Figure S1).

To gain insights into the evolution of the mineral-bound P_{org} reactant and subsequent products on an Fe oxide surface, we employed MALDI-MS to monitor the adsorbed species of the ATP reactant and its transformation products on the goethite surface as a function of time (Figure 1F). Among the Fe oxide−ribonucleotide pairings, we specifically chose the reactions of goethite and ATP for this MALDI-MS analysis due to previous reports of high reactivity of goethite with ATP.[10,17] For these MALDI-MS data, the relative intensity of each compound can be compared with itself across different times (e.g., ATP at 4 h can be compared to ATP at 1 and 7 d) but not with the intensity of another compound (e.g., ATP at 4 h should not be compared to ADP at 4 h or AMP at 4 h) (Figure 1F). From 4 h to 1 d of the ATP-goethite reaction, both ATP and AMP intensities were decreased by 30%, while the ADP intensity was decreased only by 13% (Figure 1F). After 7 d of reaction, the intensities of all three compounds on the surface were decreased by 90% or greater, relative to the intensities at 4 h (Figure 1F). The difference between the decrease in intensity of ATP and AMP compared to ADP between 4 h and 1 day of reaction time implied that both ATP and AMP were short-lived compounds on the goethite surface (Figure 1F), consistent with previous reports of mass balance of solution-based LC-MS data[10,17] that indicated the ultimate release in solution of the majority of the dephosphorylation products from the ATP-goethite reactions (Figure 1F). The rapid disappearance of surface-bound ATP was in accordance with the reported high reactivity of goethite for ATP dephosphorylation, resulting in no ATP in solution after 1 d of reaction.[17] The depletion in surface-bound AMP may be the result of AMP dephosphorylation as well as desorption because a steady increase in dissolved AMP in solution was reported during a 4-day ATP reaction with goethite[17] and AMP was found to have lower binding affinity for the goethite surface compared to ATP and ADP, likely due to the relatively lower phosphate stoichiometry of AMP for electrostatic coupling with the positively charged Fe oxide surface.[36,64] We attributed the relatively slower depletion in surface-bound ADP compared to ATP and AMP to the sustained generation of ADP from ATP, reportedly reaching a maximum concentration in solution at 1-d reaction.[17] Next, we investigated the adsorption mechanisms of monophosphorylated and triphosphorylated ribonucleotides with the three Fe oxides.

3.2. Binding Interactions at the Fe Oxide Surfaces.

The initiation of the precatalytic complex requires the formation of a ribonucleotide adsorbate with an Fe oxide surface. Therefore, we probed the binding interactions and adsorbate conformations of a monophosphorylated ribonucleotide and a triphosphorylated ribonucleotide, focusing on AMP and ATP, using solid-state ATR-FTIR data and molecular modeling simulations both as dry adsorbate systems to facilitate direct comparisons (Figure 2). With ATR-FTIR spectroscopy, we sought to identify the functional groups, as depicted in Figure 2A, that may be involved in mediating the binding of ATP, AMP, and adenine to the Fe oxide surfaces. Reference spectra[65−67] for ATP and AMP have highlighted the following relevant bands, which we subsequently followed to determine complexation mechanisms: two deformation (δ) amine bands (δNH bands, denoted a and b) at 1654 and 1596 cm^{-1} for ATP and at 1643 and 1604 cm^{-1} for AMP; a stretching (v) band for C−O (vC−O) at 1100 cm^{-1} (denoted c); a C−N band at 1245 cm^{-1} (denoted d); bands for the phosphate group at 1245 cm^{-1} (denoted d), 1001 cm^{-1} (denoted e), and 900 cm^{-1} (denoted g); and the sugar-phosphodiester band at 810 cm^{-1} for ATP and 819 cm^{-1} for AMP (denoted g) (Figure 2A−D).

The ATR-FTIR spectra for ATP and AMP adsorbed onto goethite both showed only three notable peaks, which were all shifted by 5−30 cm^{-1}: the two δNH bands (a and b) at 1665 and 1590 cm^{-1} and the vC−O band (denoted c) at 1130 cm^{-1} (Figure 2B). Thus, the adsorption interactions with goethite appeared to be mediated primarily through the amino group in the adenine base, with some contributions from the C−O

https://doi.org/10.1021/acs.est.4c12049
Environ. Sci. Technol. 2025, 59, 5568−5584

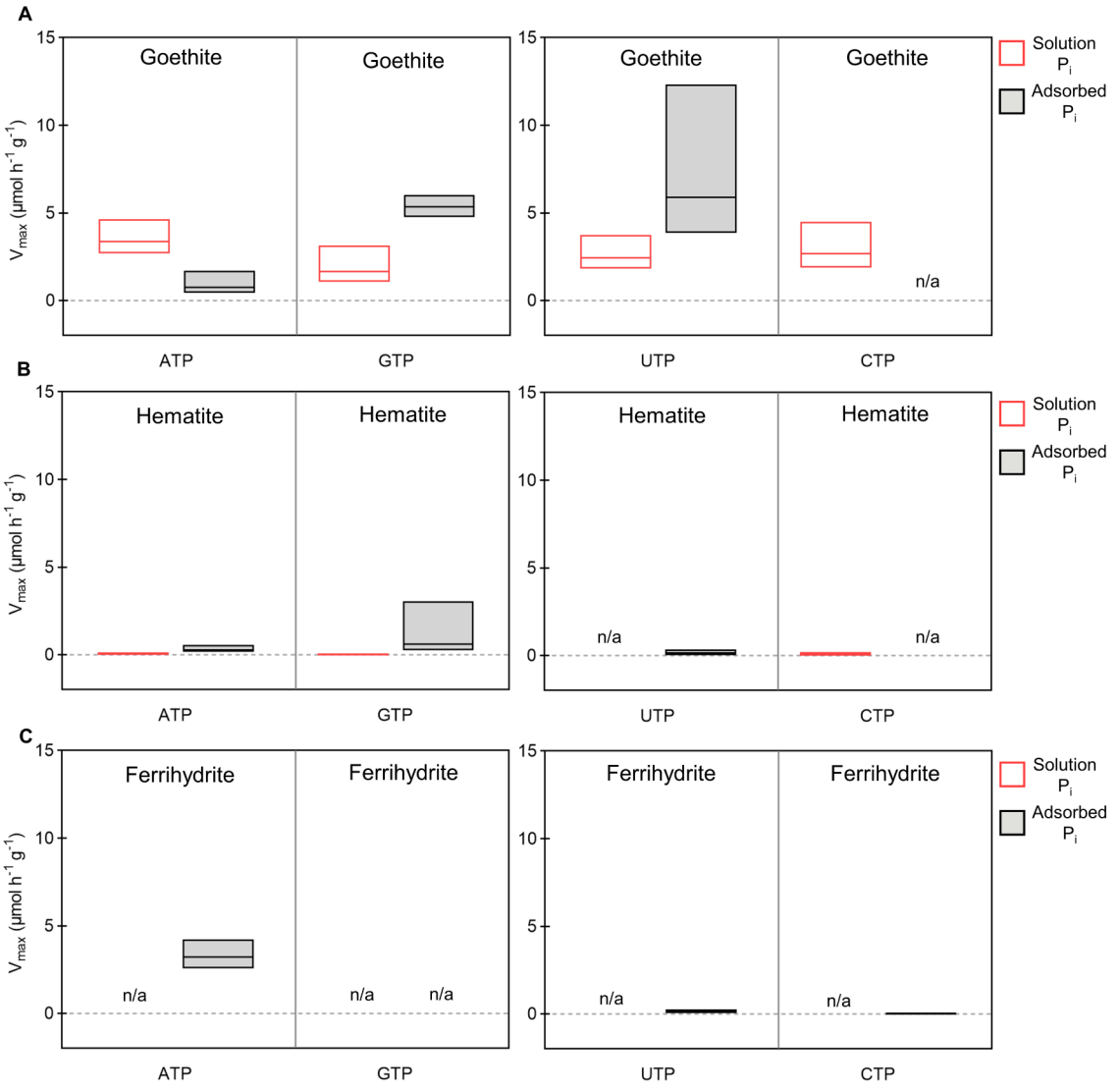

Figure 3. Dephosphorylation reactivity rates of iron oxides with triphosphorylated purine-based and pyrimidine-based ribonucleotides. Apparent maximum rate (V_{max}, μmol P_i h^{-1} $g_{mineral}{}^{-1}$) of solution P_i (white box with red outline) and adsorbed P_i (gray box with black outline) generated by dephosphorylation of (from left to right) purine-based ribonucleotides (ATP, GTP) and pyrimidine-based ribonucleotides (UTP, CTP) catalyzed by (A) goethite, (B) hematite, and (C) ferrihydrite. The box plots represent the lower and upper 95% confidence intervals and the expected V_{max} value obtained from fitting experimental data to Michaelis−Menten enzyme kinetics; V_{max} value was not available (n/a) when no P_i was detected. Data and Michaelis−Menten kinetic models are provided Figures S5−S7, Tables S12−S14, and S19−S21. The kinetic parameters and associated data for reactions of ATP with the Fe oxides were reported previously.[10]

bond present in the ribose sugar (Figure 2B). In contrast to previous evidence on adsorbed ATP and AMP on goethite,[36] we did not obtain any evidence of the contribution of phosphate groups toward the binding mechanism on this mineral (Figure 2B), which may be due to the weak absorption of phosphate on goethite, or an artifact of the background subtraction due to overlaps of the bands corresponding to the phosphate with those from the goethite mineral at the 950 to 800 cm^{-1} region that has been reported in previous ATR-FTIR spectra of goethite−phosphate complexes.[32,68,69] However, our molecular modeling simulations corroborated the lack of involvement of the phosphate group, and instead, the model adsorbate conformations predicted H-bonding only between the amino group of AMP and goethite (Figure 2B).

Compared to that of goethite, the ATR-FTIR data with both hematite and ferrihydrite implicated the involvement of additional functional groups in the ribonucleotide adsorption (Figure 2C, D). With hematite, we recorded that the band for the C−N moiety (d, at 1243 cm^{-1}), the three bands for the phosphate group (d, at 1243 cm^{-1}; e, at 997 cm^{-1}; and g, at 905 cm^{-1}), a band corresponding to an OH moiety (e at 997 cm^{-1}), and a band associated with the sugar−phosphodiester chain (g, at 815 cm^{-1}) were subjected to a small shift (less than 5 cm^{-1}), suggesting minor contributions of these functional groups (Figure 2C). However, a significant (30 cm^{-1}) shift in the C−O band implied a relatively greater involvement in the adsorption of the ribonucleotide onto the hematite surface (Figure 2C). In agreement with the ATR-FTIR data, the binding mechanisms in the optimized model adsorbates with hematite revealed H-bonds between organic moieties in both ribonucleotide reactants (i.e., AMP and ATP) with the mineral surface, in addition to the phosphate group in the case of ATP (Figure 2E). The H-bonding interactions on the hematite surface were through N atoms in the amino moiety and

https://doi.org/10.1021/acs.est.4c12049
Environ. Sci. Technol. 2025, 59, 5568−5584

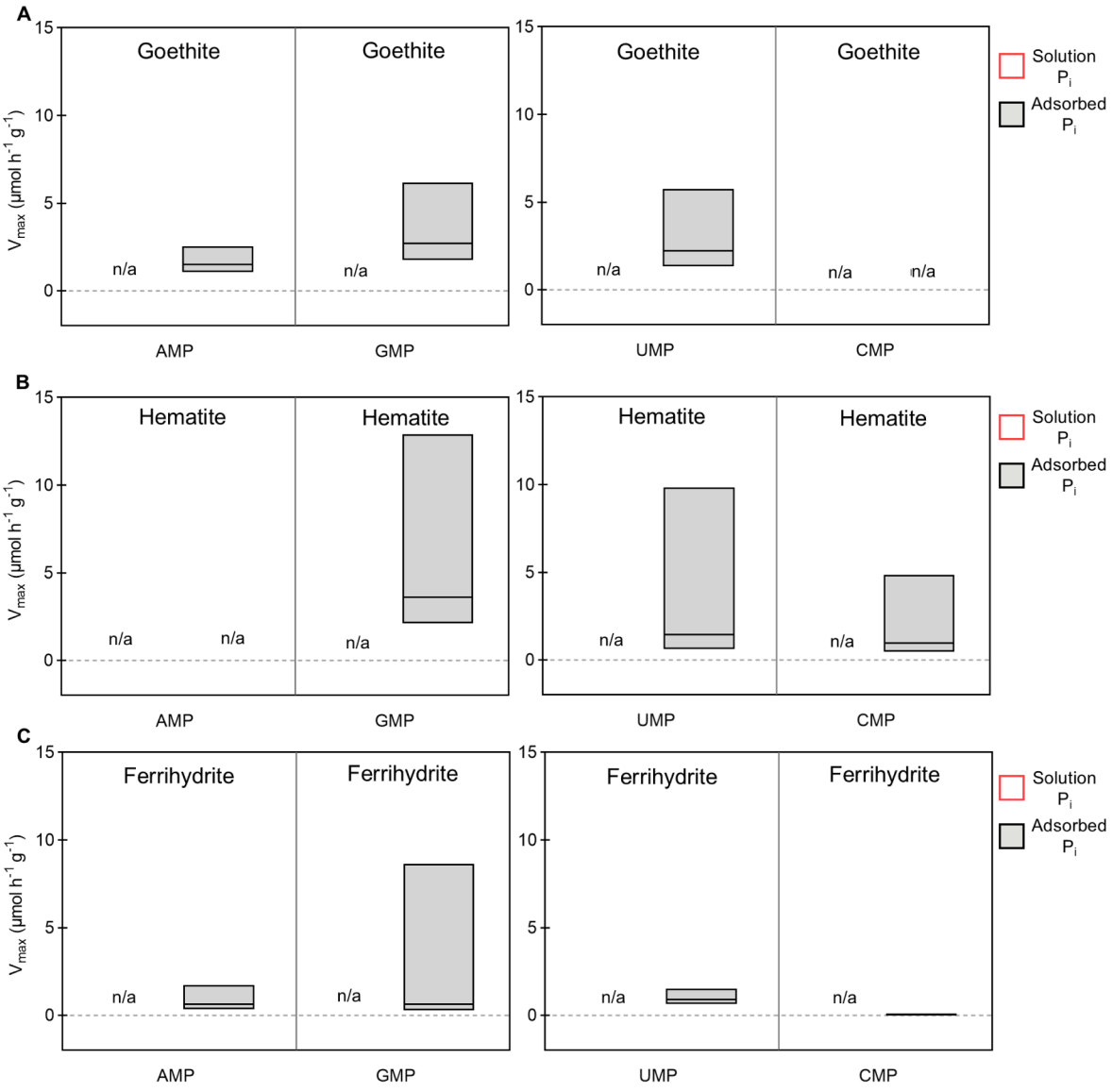

Figure 4. Dephosphorylation reactivity rates of iron oxides with monophosphorylated purine-based and pyrimidine-based ribonucleotides. Apparent maximal rate (V_{max}, μmol P_i h^{-1} $g_{mineral}^{-1}$) of solution P_i (white box with red outline) and adsorbed P_i (gray box with black outline) generated by dephosphorylation of (from left to right) purine-based ribonucleotides (AMP, GMP) and pyrimidine-based ribonucleotides (UMP, CMP) catalyzed by (A) goethite, (B) hematite, and (C) ferrihydrite. The box plots represent the lower and upper 95% confidence intervals and the expected V_{max} value obtained from fitting experimental data to Michaelis−Menten enzyme kinetics; V_{max} value was not available (n/a) when no P_i was detected. Data and Michaelis−Menten kinetic models are provided in Figures S8−S11 and Tables S15−S21.

heterocyclic nitrogenous ring of the adenine base and oxygen atoms in both the OH group and sugar ring of the ribose sugar (Figure 2E). In contrast to the molecular simulation results with hematite, the involvement of the amino group in adenine was not captured by the ATR-FTIR data, likely due to low resolution in the 1700 to 1400 cm^{-1} region of the spectra that overlapped with the N−H stretching band (Figure 2E). In summary, the molecular modeling with hematite predicted 14 H-bonds for ATP and six H-bonds for AMP binding on hematite, thus implying a relatively greater binding affinity of ATP than AMP for the hematite surface (Figure 2E).

For the adsorption of ATP and AMP on ferrihydrite, the ATR-FTIR data captured strong involvement of an amino group (a, shift by 8 cm^{-1} in one of the δNH bands), a nucleobase moiety (h, shifted by 13 cm^{-1} from the C−N band), the sugar OH moiety (c, shifted by 30 cm^{-1} of the C−O band), and the phosphate group[65,66] (i, shifted by 11 cm^{-1} for ATP and by 5 cm^{-1} for AMP; j, shifted by 3 cm^{-1}) (Figure 2F). Our molecular simulations predicted the formation of H-bonds to the ferrihydrite surface through both the phosphate and OH moieties of ATP and AMP, corroborating previous binding studies[14,31,36] that emphasized the important involvement of the phosphate moiety in the binding of ribonucleotides to the ferrihydrite surface. Additionally, in agreement with our ATR-FTIR data, our modeling data highlighted the importance of the amino moiety and the N atoms of the heterocyclic nitrogenous ring of the adenine base and the OH groups of the ribose sugar (Figure 2G). We acknowledge that water bridges may be involved in the binding of and transformation of compounds by Fe oxides.[70,71] Therefore, future studies should consider hydrated systems in elucidating binding interactions at water−mineral interfaces and the subsequent implications for the catalytic reaction mechanism. Here, the dry systems of both the experimentally determined

https://doi.org/10.1021/acs.est.4c12049
Environ. Sci. Technol. 2025, 59, 5568−5584

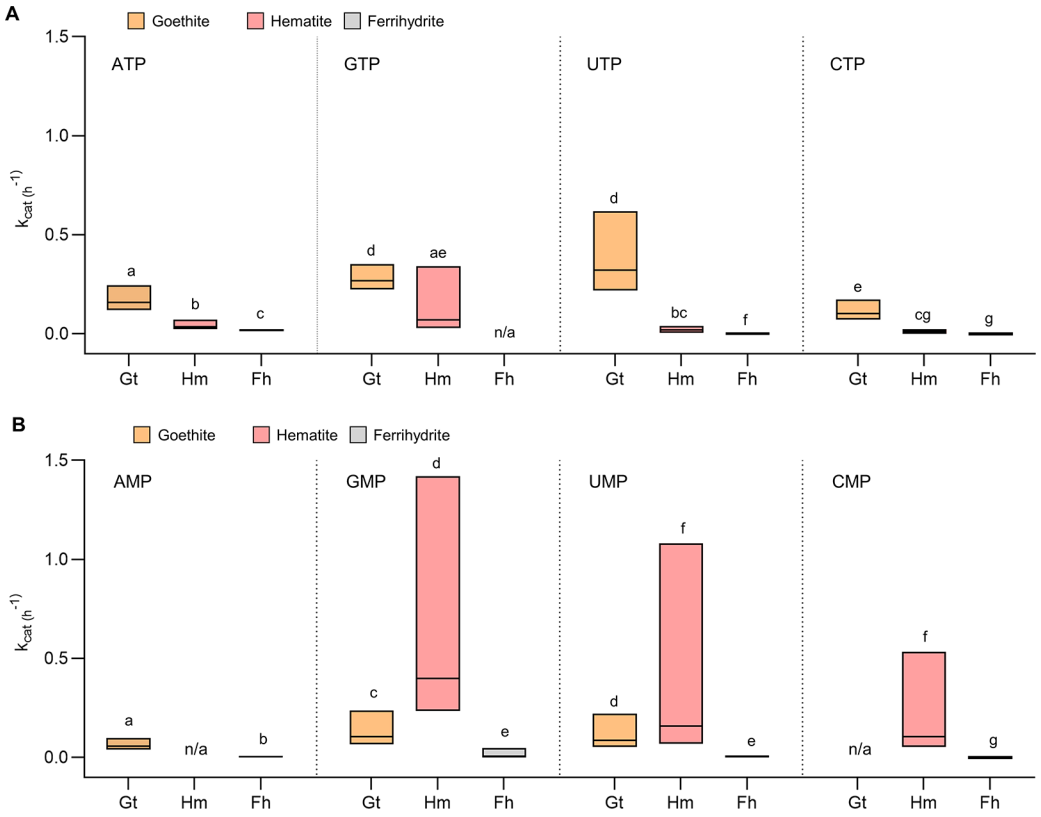

Figure 5. Catalytic turnover number of iron oxides for the dephosphorylation of purine-based and pyrimidine-based ribonucleotides. Apparent total turnover number (total k_{cat}, h^{-1}) of (A) triphosphorylated ribonucleotides and (B) monophosphorylated ribonucleotides for each Fe oxide: goethite (gold), hematite (pink), and ferrihydrite (gray). Each k_{cat} value was calculated by normalizing the sum of the V_{max} values, when both solution P_i and adsorbed P_i were detected, by the density of P_i binding sites (μmol P_i^{-1} $g_{mineral}^{-1}$) for each mineral. Statistical significance is represented by the lettering above each value ($p < 0.05$), calculated using the *F*-test; n/a denotes no available V_{max} values for k_{cat} calculations. The kinetic parameters for reactions of ATP with the Fe oxides were reprinted from a data set published previously.[14]

FTIR data and the theoretical model of the ribonucleotide−Fe oxide complex illustrated adsorbate conformations with corroborating binding interactions.

3.3. Kinetic Benchmarking of Phosphatase-Mimetic Reactivity of Fe Oxides. *3.3.1. Maximal Production Rates or V_{max}.* We determined the kinetics of the reactions of the ribonucleotides with goethite, hematite, and ferrihydrite and compared these results to the reported[10] values for reactions of ATP with Fe oxides. To acknowledge the evolution of both solution P_i and mineral surface-localized P_i, we determined a V_{max} for P_i measured in solution (termed solution V_{max}) and a V_{max} for P_i accumulated on the mineral surface as determined by XANES analysis (termed adsorbed V_{max}). Only goethite reactions with the triphosphorylated ribonucleotides led to the production of significant P_i in solution (Figure 3A). Reported reactions of ATP with goethite[10] exhibited the highest solution V_{max} (2.70−4.65 P_i h^{-1} g^{-1} goethite), which was 50% higher than with GTP (1.08−3.15 P_i h^{-1} g^{-1} Gt; $p < 0.05$), and about 20% higher than with UTP and CTP (1.82−4.49 P_i h^{-1} g^{-1} goethite, $p < 0.01$) (Figure 3A and Table S19). By comparison, with hematite, the solution V_{max} was reported to be minimal with ATP[10] (0.05−0.08 P_i h^{-1} g^{-1} hematite), as found here with CTP (0.01−0.22 P_i h^{-1} g^{-1} hematite, $p < 0.01$), and no solution P_i was detected in GTP and UTP reactions with hematite (Figure 3B and Table S20). Additionally, for the reactions with ferrihydrite, none of the triphosphorylated ribonucleotides generated P_i in solution (Figure 3C and Table S21), including previously reported reactions of ATP with ferrihydrite.[10]

In contrast to the mineral-dependent detection of dissolved P_i, all three Fe oxides exhibited some catalytic reactivity in the form of adsorbed P_i produced from various triphosphorylated ribonucleotides. Goethite expressed a range of mineral surface-based V_{max} with the triphosphorylated ribonucleotides above the reported[10] value with ATP (0.45−1.70 μmol P_i h^{-1} g^{-1} goethite) and up to 12.33 μmol P_i h^{-1} g^{-1} goethite (Figure 3A), which was 3-fold to 30-fold higher than the surface-based V_{max} recorded previously,[10] with hematite (0.16−0.58 μmol P_i h^{-1} g^{-1} hematite, $p < 0.01$; Figure 3B and Table S20). Ferrihydrite was reported[10] to show appreciable surface-based reactivity with ATP (2.59−4.24 μmol P_i h^{-1} g^{-1} ferrihydrite); however, this value was minimal with the other triphosphorylated ribonucleotides investigated here (<0.25 μmol P_i h^{-1} g^{-1} ferrihydrite; $p < 0.01$) (Figure 3C and Table S21). Of the Fe oxides, goethite exhibited the highest V_{max} values due to the summation of the solution-based and surface-based P_i generation from triphosphorylated ribonucleotides (Figure 3C).

With respect to the dephosphorylation kinetics of monophosphorylated ribonucleotides, they were distinct from those of their triphosphorylated counterparts (Figure 4). Notably, potentially due to the higher energy requirement for breaking phosphomonoester bonds compared to phosphoanhydride bonds,[72] no P_i was detected in solution during the reactions of the monophosphorylated ribonucleotides with the three Fe

https://doi.org/10.1021/acs.est.4c12049
Environ. Sci. Technol. 2025, 59, 5568−5584

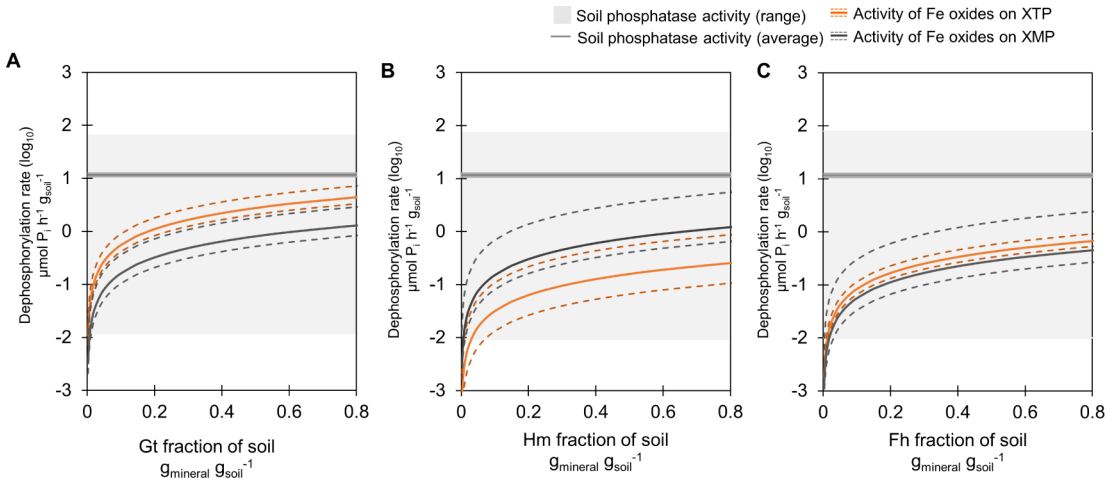

Figure 6. Comparison between reported soil enzymatic rates versusand iron oxide-catalyzed dephosphorylation rates. The rate of Fe oxide-catalyzed dephosphorylation (μmol P_i h^{-1} g_{soil}^{-1}, in $\log_{10}$ scale) of the combined triphosphorylated (orange) and combined monophosphorylated (gray) ribonucleotides as a function of Fe oxide fraction in soil for (A) goethite, (B) hematite, and (C) ferrihydrite. Dashed lines show the upper and lower 95% confidence intervals for the combined dephosphorylation rate of all triphosphorylated ribonucleotide (collectively referred to as XTP; orange) and monophosphorylated ribonucleotide (collectively referred to as XMP; gray) dephosphorylation. The black horizontal line depicts the reported[14] averaged enzymatic dephosphorylation rate (11.6 ± 0.8 μmol P_i h^{-1} g_{soil}^{-1}; acid and alkaline phosphatases); the light gray box shows the range of reported[14] global soil enzymatic rates.

oxides, and thus, only adsorbed V_{max} was determined (except for AMP with hematite and CMP with goethite, where no adsorbed P_i was detected) (Figure 4A,B, Tables S19 and S20). Interestingly, in contrast to the lack of solution V_{max} for GTP reacted with hematite, reactions of GMP with hematite exhibited the highest adsorbed V_{max} values (2.14−12.91 μmol P_i h^{-1} g^{-1} hematite), which were 30% higher than the adsorbed V_{max} for the GMP reaction with goethite (1.76−6.18 μmol P_i h^{-1} g^{-1} goethite; $p < 0.05$) and about 6-fold higher than the GMP reaction with ferrihydrite (0.63−8.64 μmol P_i h^{-1} g^{-1} ferrihydrite; $p < 0.001$) (Figure 4A,−C; Tables S19−S21). However, the adsorbed V_{max} value for UMP reacted with hematite (0.64−9.84 μmol P_i h^{-1} g^{-1} hematite) was comparable to the rate with goethite (1.36−5.76 μmol P_i h^{-1} g^{-1} goethite; $p = 0.42$) and ferrihydrite (0.65−1.52 μmol P_i h^{-1} g^{-1} ferrihydrite; $p = 0.06$) (Figure 4A−C and Tables S19−S21). The adsorbed V_{max} values for UMP and CMP reactions with hematite were 2-fold to 4-fold lower than the corresponding values obtained from the GMP-hematite reactions (Figure 4B and Table S20). With goethite, we obtained comparable adsorbed V_{max} values for the reactions with GMP (1.76−6.18 μmol P_i h^{-1} g^{-1} goethite) and UMP (1.36−5.76 μmol P_i h^{-1} g^{-1} goethite) ($p = 0.73$), both of which were more than 45% higher than the adsorbed V_{max} for the AMP−goethite reaction (1.06−2.56 μmol P_i h^{-1} g^{-1} goethite) ($p < 0.05$) (Figure 4A and Table S19). While V_{max} values present useful parameters for comparing the reactivity on a per-mass basis, the k_{cat} values are the appropriate parameters for probing catalytic efficiency by accounting for the density of active sites.

3.3.2. Catalytic Turnover Rates or k_{cat}. Here, as demonstrated previously,[10] we determined the k_{cat} of each ribonucleotide−Fe oxide pair by dividing the summed solution V_{max} and adsorbed V_{max} by the reported site density of P_i binding for each Fe oxide:[10,17] 26.0 ± 1.2 μmol P_i g^{-1} goethite, 9.1 ± 0.9 μmol P_i g^{-1} hematite, and 184.1 ± 6.0 μmol P_i g^{-1} ferrihydrite. Compared to the specific surface area of the mineral, the P_i binding site density was reported to be a better predictor of the affinity of the Fe oxide surface for P adsorption because it accounts for both the adsorption reactivity and the available surface area of the mineral.[17] While it exhibited the highest site density for P_i binding, ferrihydrite was the least efficient Fe oxide catalyst for both triphosphorylated and monophosphorylated ribonucleotides (Figure 5). For the triphosphorylated ribonucleotides, goethite was the most efficient Fe oxide catalyst, with k_{cat} values (0.07−0.62 h^{-1}) >68% higher than hematite (0.00−0.34 h^{-1}; $p < 0.001$) and >95% higher than ferrihydrite (0.00−0.02 h^{-1}; $p < 0.001$) (Figure 5A). For the monophosphorylated ribonucleotides, hematite exhibited the highest k_{cat} (0.00−1.41 h^{-1}), >45% higher than goethite (0.00−0.24 h^{-1}; $p < 0.05$) and >95% higher than ferrihydrite (0.00−0.05 h^{-1}; $p < 0.01$) (Figure 5B).

3.3.3. Estimations of Fe Oxide-Catalyzed Dephosphorylation in Soils with Varying Fe Oxide Content. Based on the rates obtained on a per-mass basis (i.e., V_{max}), we estimated the dephosphorylation rates in soils containing varying fractions of each Fe oxide and compared these estimations with reported phosphatase rates from soils globally[73] (Figure 6). We predicted that goethite-catalyzed rates for triphosphorylated ribonucleotides in a soil would reach within 1 order of magnitude of the averaged enzymatic P_i generation at a goethite content of >10% of the total soil by mass. Due to lower rates of P_i generation from monophosphorylated ribonucleotides compared to the triphosphorylated ribonucleotides, a goethite content of >25% of the total soil by mass would be needed to achieve comparable rates to enzymatic rates with monophosphorylated ribonucleotides (Figure 6A). The same content (>25% of the soil by mass) was estimated to be required for ferrihydrite to generate P_i from monophosphorylated ribonucleotides within 1 order of magnitude of the averaged soil enzymatic rates, whereas the relatively more reactive hematite would only need to constitute >15% of the soil by mass (Figure 6B,C). Relative to goethite, hematite and ferrihydrite were much less reactive with triphosphorylated ribonucleotides, thus requiring the soil content to be more than 80% hematite or ferrihydrite to obtain rates comparable

https://doi.org/10.1021/acs.est.4c12049
Environ. Sci. Technol. 2025, 59, 5568−5584

to reported average values for enzyme activity (Figure 6B,C). Given a reported Fe oxide content of about 20% on a per-mass basis in certain high-Fe containing soils and sediments,[7−9] our data implied that abiotic rates from Fe oxides have the potential to generate P_{org}-derived P_i alongside enzymes in the P cycle in these environments,[10] albeit the potential effects of organic matter coatings of soil minerals on our estimated rates remained to be examined. In environments enriched in Fe oxides and other minerals, enzyme activity may be limited due to enzyme adsorption onto mineral surfaces,[74,75] thereby further highlighting the importance of accounting for the abiotic contributions in P recycling catalyzed by Fe oxides in these environments.

3.4. Insights into the Dependence of Phosphatase-Mimetic Reactivity on Mineral and Reactant Structures and Environmental Implications. *3.4.1. Effect of Mineral Crystallinity on Catalytic Efficiency.* Our data stressed that the surface area of reactive minerals such as Fe oxides was not a good predictor of the efficiency of the catalytic reactivity. Ferrihydrite, the semicrystalline Fe oxide with the highest surface area amongst the three minerals in our investigation. However, after normalizing V_{max} by the P_i binding capacity, the resulting k_{cat} values revealed that the crystalline Fe oxides express higher dephosphorylation efficiency than ferrihydrite. Surface acidity of the mineral has been proposed to mediate the dephosphorylation reaction catalyzed by Fe oxides. Specifically, the content of Lewis acid sites has been linked to the enhanced reactivity of hematite and goethite.[15] In fact, the Lewis acid site was reported to act as the catalytic center of Fe oxide-mediated oxidation reactions.[15,70,76,77] However, like surface area, the concentration of Lewis acid sites may not fully explain mineral reactivity. For instance, while hematite was reported to possess ∼20% more Lewis acid sites than goethite, hematite displayed approximately 75% lower dephosphorylation of synthetic *p*NPP.[15] Mineral characteristics such as surface wetting[71] or the position of Fe (III) centers in the mineral structure[13] may also influence reactivity. Thus, further investigations are needed to determine the extent to which Lewis acid sites and other surface properties control the reactivity of Fe oxides toward P_{org} compounds.

3.4.2. Reactivity of Compounds with Phosphoester, Phosphodiester, and Phosphoanhydride Bonds. Phosphomonoesters, which are P_{org} compounds with phosphoester bonds, are reported to accumulate in environmental matrices.[43,78,79] Previous studies with a single P_{org} concentration[10,14,17] have demonstrated preferential dephosphorylation of phosphoanhydride bonds over phosphoester bonds by goethite and hematite. Here, our kinetics data over a wide range of P_{org} concentrations revealed that the three Fe oxides trapped all the P_i generated during the dephosphorylation of the monophosphorylated ribonucleotides. Therefore, in addition to dissolved P_i, produced P_i from ribonucleotides that remains bound on the Fe oxide surface may provide a bioavailable P source after desorption from the mineral or mineral dissolution.

3.4.3. Weak Adsorption and High Catalytic Efficiency. Among the investigated Fe oxides, goethite exhibited the highest k_{cat} toward AMP and ATP, but these adsorptives displayed the fewest intermolecular interactions with the goethite surface. Therefore, we propose that the surface chemistry may drive the catalytic reactivity of the Fe oxides by modulating the extent of adsorption. Interestingly, we obtained a greater than 2-fold higher k_{cat} for ATP than for AMP reacted with goethite, and the molecular modeling highlighted a H-bonding between the adenine base and the mineral surface to anchor the bound AMP, an interaction that was absent in the ATP−goethite complex. The lack of H-bonding through the adenine base in the latter complex may be due to limitations in the structural flexibility of ATP, especially given the orientation of all three phosphate groups toward the mineral surface that may prevent the required orientation of the nucleobase to form H-bonding interactions with the mineral. These latter findings were thus in agreement with an inverse relationship between the binding affinity and catalytic reactivity. However, our data were not consistent with those from Li et al.,[15] which reported 2-fold higher rates of *p*NPP dephosphorylation by goethite faces that facilitated relatively stronger binding as indicated by ∼15% greater adsorption energy. Ribonucleotides and *p*NPP are structurally different compounds; there is no biological analog to *p*NPP. The difference between the nucleobase in ribonucleotides, which is a bulkier organic moiety containing several functional groups, and the nitrobenzyl ring in *p*NPP may influence the conformation of the P_{org}−Fe oxide complex and the resulting catalysis.[80] Therefore, direct comparisons to naturally occurring P_{org} compounds should not be made. Our findings with naturally occurring compounds such as ribonucleotides suggested a threshold at which the extent of the binding affinity of the P_{org} reactant to the mineral surface would be inhibitory to the catalytic reaction.

3.4.4. Environmental Implications. In agricultural soils, standard practices rely heavily on P_i fertilizers to meet crop needs.[81] However, plants only take up 10−15% of any given year's applied P, thereby relying instead on legacy P stored in soils to meet P requirements.[82] This legacy P includes P_{org} from plant and microbial biomass and P_i primarily from previous fertilizer applications. In fact, up to half of the legacy P in soils is in P_{org} forms.[83] Consequently, assessments of global food security stress the need to advance our understanding of the biogeochemical recycling of P_{org}, as legacy P_{org} is much less well studied than P_i.[84] Prior studies have proposed the addition of Fe oxides as abiotic catalysts, beyond serving as only adsorbents, in P cycling in soil and sediment environments.[1,10,16] Here, for the first time, we provide detailed quantitative benchmarking of this abiotic catalysis on structurally different P_{org} compounds by exploring the dephosphorylation kinetics of eight different ribonucleotides by three Fe oxides. We identified the varying involvement of the phosphate group, sugar hydroxyl moieties, and the nitrogenous ring and amino moiety in the nucleobase in mediating the mechanisms of adsorption onto the different Fe oxide surfaces. Importantly, we found that triphosphorylated ribonucleotides, which contain a phosphoanhydride bond, and monophosphorylated ribonucleotides, which contain a monoester bond, were both dephosphorylated by Fe oxides at rates comparable to the reported rates of soil phosphatases.[73] Given the ubiquitous detection of phosphomonoesters in soils,[85,86] it is worthwhile to determine the kinetic parameters for the dephosphorylation of other phosphomonoesters such as phytate and glucose-6-phosphate, which were found to undergo minimal to no dephosphorylation by Fe oxides at a single μM reactant concentration[10] or exhibit appreciable to significant dephosphorylation at a single mM reactant concentration.[16] Furthermore, the possible Fe oxide-catalyzed production of P_i from other common P_{org} compounds with phosphodiester bonds such as phospholipids and nucleic acids (i.e., DNA and RNAs) remains underexplored, both of which

https://doi.org/10.1021/acs.est.4c12049
Environ. Sci. Technol. 2025, 59, 5568−5584

can produce phosphomonoesters during abiotic or biotic degradation.[47,87] Thus, Fe oxide-catalyzed dephosphorylation of the phosphomonoester pool can potentially constitute an important contribution to the conversion of P_{org} to P_i in the global P cycle.

We posit that the accounting of environmental P fluxes is currently incomplete due to the exclusion of Fe oxides and other reactive mineral oxides,[13,16,17] especially given our aforementioned estimations that Fe oxide-catalyzed dephosphorylation rates at relevant soil Fe oxide content may be comparable to reported rates of phosphorus-recycling enzymes in soils. Our findings contribute to the mounting evidence on the catalytic reactivity of goethite,[10,13,15,17] hematite,[10,13,15−17] and ferrihydrite,[10,13,14,17] all of which support the inclusion of these minerals as catalysts of organic P recycling in P cycling models. In addition to the reactivity investigated here in the absence of light, goethite and ferrihydrite were reported to transform ATP through photolysis in the presence of light.[88] Therefore, these photocatalytically reactive minerals can potentially further contribute to the abiotic generation of P_i in sunlight-exposed environments such as shallow lakes.[89] Manganese oxides, which are often present at relatively ∼10-fold lower concentrations than Fe oxides in soil[90,91] and sediment[91,92] environments, represent another reactive mineral oxide of interest. Manganese oxide can also catalyze the production of P_i from P_{org} compounds via both hydrolysis[13,16,17,64] and transformation of organic matter through redox reactions.[93,94] Investigations of the catalytic parameters for dephosphorylation reactions by manganese oxides are warranted. Furthermore, to complete a comprehensive evaluation of the abiotic contribution of Fe oxides in environmental matrices by building on the present study, future work needs to address the effects of natural organic matter[95] and plant-derived small carboxylic acids[96,97] on the kinetic catalytic parameters of the Fe oxides determined here. In support of the persistence of the catalytic reactivity of Fe oxides in environmental matrices, a recent study[10] with natural soil and sediment samples identified that the small fraction of Fe oxides (≤ ∼20%) in these heterogeneous samples was responsible for the catalytic reactivity toward ribonucleotides. Future studies on contextualizing the kinetic parameters such as those provided here for the transformation of various P_{org} compounds catalyzed by Fe oxides within complex environmental matrices will be instrumental in advancing a modeling of the budget for both abiotic and biotic catalysts in environmental P cycling.

■ ASSOCIATED CONTENT

Supporting Information

The Supporting Information is available free of charge at https://pubs.acs.org/doi/10.1021/acs.est.4c12049.

Tables S1−S21: chemicals used for experiments, structural data of ribonucleotides for simulated adsorption, adsorbed P data, XANES LCF fractions with fitting errors, solution data for each ribonucleotide and Fe oxide reaction from colorimetric and LC-MS analyses, and the resulting kinetic parameters for the dephosphorylation reactions; Figures S1−S11: XANES LCF fractions with fitting errors for each ribonucleotide and Fe oxide reaction and Michaelis−Menten-type kinetic modeling of the Fe oxide-catalyzed dephosphorylation kinetics (PDF)

Kinetics data (XLSX)

■ AUTHOR INFORMATION

Corresponding Author

Ludmilla Aristilde − *Department of Civil and Environmental Engineering, Northwestern University, Evanston, Illinois 60208, United States;* orcid.org/0000-0002-8566-1486; Phone: 847-491-2999; Email: ludmilla.aristilde@northwestern.edu

Authors

Jade J. Basinski − *Department of Civil and Environmental Engineering, Northwestern University, Evanston, Illinois 60208, United States*

Sharon E. Bone − *Stanford Synchrotron Radiation Light Source, SLAC National Accelerator Laboratory, Menlo Park, California 94025, United States*

Aurore Niyitanga Manzi − *Department of Civil and Environmental Engineering, Northwestern University, Evanston, Illinois 60208, United States*

Nasrin Naderi Beni − *Department of Civil and Environmental Engineering, Northwestern University, Evanston, Illinois 60208, United States*

Fernando R. Tobias − *Department of Chemistry, Northwestern University, Evanston, Illinois 60208, United States; Integrated Molecular Structure Education and Research Center, Northwestern University, Evanston, Illinois 60208, United States;* orcid.org/0000-0002-4085-4188

Marcos Sanchez − *Department of Civil and Environmental Engineering, Northwestern University, Evanston, Illinois 60208, United States*

Cynthia X. Cheng − *Department of Civil and Environmental Engineering, Northwestern University, Evanston, Illinois 60208, United States*

Wiriya Thongsomboon − *Department of Civil and Environmental Engineering, Northwestern University, Evanston, Illinois 60208, United States;* Present Address: Department of Chemistry, Mahasarakham University, Mahasarakham, 44150, Thailand

Complete contact information is available at: https://pubs.acs.org/10.1021/acs.est.4c12049

Notes

The authors declare no competing financial interest.

■ ACKNOWLEDGMENTS

This material is based upon work supported by the U.S. Department of Energy, Office of Science, Office of Basic Energy Sciences, Geosciences program, under award number DE-SC0021172. Use of the Stanford Synchrotron Radiation Lightsource, SLAC National Accelerator Laboratory, is supported by the U.S. Department of Energy, Office of Science, Office of Basic Energy Sciences, under contract no. DE-AC02-76SF00515. This research was supported in parts by a grant from the Northwestern International Institute in Nanotechnology. We thank Dr. Kevin Rosso and Dr. Michel Sassi of the Pacific Northwest National Laboratory for providing their published ferrihydrite structure used to build the final ferrihydrite structure used here in our molecular simulations. We are grateful to Yeonsoo Park of the Aristilde Research Group at Northwestern University for her valuable preliminary experiments in the initial stages of this project.

REFERENCES

(1) Duhamel, S.; Diaz, J. M.; Adams, J. C.; Djaoudi, K.; Steck, V.; Waggoner, E. M. Phosphorus as an Integral Component of Global Marine Biogeochemistry. *Nat. Geosci.* **2021**, *14* (6), 359−368.

(2) Achat, D. L.; Pousse, N.; Nicolas, M.; Brédoire, F.; Augusto, L. Soil Properties Controlling Inorganic Phosphorus Availability: General Results from a National Forest Network and a Global Compilation of the Literature. *Biogeochemistry* **2016**, *127* (2), 255−272.

(3) Berner, R. A. Phosphate Removal from Sea Water by Adsorption on Volcanogenic Ferric Oxides. *Earth Planet. Sci. Lett.* **1973**, *18* (1), 77−86.

(4) Ruttenberg, K. C.; Sulak, D. J. Sorption and Desorption of Dissolved Organic Phosphorus onto Iron (Oxyhydr)Oxides in Seawater. *Geochim. Cosmochim. Acta* **2011**, *75* (15), 4095−4112.

(5) Herndon, E. M.; Kinsman-Costello, L.; Duroe, K. A.; Mills, J.; Kane, E. S.; Sebestyen, S. D.; Thompson, A. A.; Wullschleger, S. D. Iron (Oxyhydr)Oxides Serve as Phosphate Traps in Tundra and Boreal Peat Soils. *J. Geophys. Res.: Biogeosci.* **2019**, *124* (2), 227−246.

(6) Berens, M. J.; Michaud, A. B.; VanderJeugdt, E.; Miah, I.; Sutor, F. W.; Emerson, D.; Bowden, W. B.; Kinsman-Costello, L.; Weintraub, M. N.; Herndon, E. M. Phosphorus Interactions with Iron in Undisturbed and Disturbed Arctic Tundra Ecosystems. *Environ. Sci. Technol.* **2024**, *58* (26), 11400−11410.

(7) Uzarowicz, Ł.; Zagorski, Z. Mineralogy and Chemical Composition of Technogenic Soils (Technosols) Developed from Fly Ash and Bottom Ash from Selected Thermal Power Stations in Poland. *Soil Sci. Annual* **2015**, *66*, 82−91.

(8) Thorpe, M. T.; Hurowitz, J. A.; Dehouck, E. Sediment Geochemistry and Mineralogy from a Glacial Terrain River System in Southwest Iceland. *Geochim. Cosmochim. Acta* **2019**, *263*, 140−166.

(9) Cornell, R. M.; Schwertmann, U. Soils. In *The Iron Oxides*; John Wiley & Sons, Ltd, 2003, pp. 433−474. DOI: .

(10) Basinski, J. J.; Bone, S. E.; Klein, A. R.; Thongsomboon, W.; Mitchell, V.; Shukle, J. T.; Druschel, G. K.; Thompson, A.; Aristilde, L. Unraveling Iron Oxides as Abiotic Catalysts of Organic Phosphorus Recycling in Soil and Sediment Matrices. *Nat. Commun.* **2024**, *15* (1), 5930.

(11) Harrison, A. F. *Soil Organic Phosphorus. A Review of World Literature*; CAB International: Wallingford, 1987.

(12) Ahlgren, J.; Tranvik, L.; Gogoll, A.; Waldebäck, M.; Markides, K.; Rydin, E. Sediment Depth Attenuation of Biogenic Phosphorus Compounds Measured by 31P NMR. *Environ. Sci. Technol.* **2005**, *39* (3), 867−872.

(13) Baldwin, D. S.; Beattie, J. K.; Coleman, L. M.; Jones, D. R. Phosphate Ester Hydrolysis Facilitated by Mineral Phases. *Environ. Sci. Technol.* **1995**, *29* (6), 1706−1709.

(14) Klein, A. R.; Bone, S. E.; Bakker, E.; Chang, Z.; Aristilde, L. Abiotic Phosphorus Recycling from Adsorbed Ribonucleotides on a Ferrihydrite-Type Mineral: Probing Solution and Surface Species. *J. Colloid Interface Sci.* **2019**, *547*, 171−182.

(15) Li, T.; Zhong, W.; Jing, C.; Li, X.; Zhang, T.; Jiang, C.; Chen, W. Enhanced Hydrolysis of P-Nitrophenyl Phosphate by Iron (Hydr)Oxide Nanoparticles: Roles of Exposed Facets. *Environ. Sci. Technol.* **2020**, *54* (14), 8658−8667.

(16) Wan, B.; Huang, R.; Diaz, J. M.; Tang, Y. Rethinking the Biotic and Abiotic Remineralization of Complex Phosphate Molecules in Soil and Sediments. *Sci. Total Environ.* **2022**, *833*, 155187.

(17) Klein, A. R.; Basinski, J. J.; Niyitanga Manzi, A.; Cheng, C. X.; Sanchez, M.; Thongsomboon, W.; Aristilde, L. Phosphorus Recycling by Mineral-Catalyzed Ribonucleotide Cleavage on Iron and Manganese Oxides. *Environ. Chem. Lett.* **2024**, *22*, 2627.

(18) Cornell, R. M.; Schwertmann, U. Introduction to the Iron Oxides. In *The Iron Oxides: structure, Properties, Reactions, Occurrences and Uses*; John Wiley & Sons, Ltd, 2003, pp. 1−7. .

(19) Kiem, R.; Kögel-Knabner, I. Refractory Organic Carbon in Particle-Size Fractions of Arable Soils II: Organic Carbon in Relation to Mineral Surface Area and Iron Oxides in Fractions < 6 Mm. *Org. Geochem.* **2002**, *33* (12), 1699−1713.

(20) Chen, C.; Barcellos, D.; Richter, D. D.; Schroeder, P. A.; Thompson, A. Redoximorphic Bt Horizons of the Calhoun CZO Soils Exhibit Depth-Dependent Iron-Oxide Crystallinity. *J. Soils Sediments* **2019**, *19* (2), 785−797.

(21) Thompson, A.; Chadwick, O. A.; Rancourt, D. G.; Chorover, J. Iron-Oxide Crystallinity Increases during Soil Redox Oscillations. *Geochim. Cosmochim. Acta* **2006**, *70* (7), 1710−1727.

(22) Jambor, J. L.; Dutrizac, J. E. Occurrence and Constitution of Natural and Synthetic Ferrihydrite, a Widespread Iron Oxyhydroxide. *Chem. Rev.* **1998**, *98* (7), 2549−2586.

(23) Wang, H. D.; White, G. N.; Turner, F. T.; Dixon, J. B. Ferrihydrite, Lepidocrocite, and Goethite in Coatings from East Texas Vertic Soils. *Soil Sci. Soc. Am. J.* **1993**, *57* (5), 1381−1386.

(24) Langmuir, D. *Aqueous Environmental Geochemistry*; Prentice Hall: Upper Saddle River, N.J, 1997.

(25) Solhtalab, M.; Klein, A. R.; Aristilde, L. Hierarchical Reactivity of Enzyme-Mediated Phosphorus Recycling from Organic Mixtures by Aspergillus Niger Phytase. *J. Agric. Food Chem.* **2021**, *69* (7), 2295−2305.

(26) Khare, N.; Hesterberg, D.; Beauchemin, S.; Wang, S.-L. XANES Determination of Adsorbed Phosphate Distribution between Ferrihydrite and Boehmite in Mixtures. *Soil Sci. Soc. Am. J.* **2004**, *68* (2), 460−469.

(27) Georgelin, T.; Jaber, M.; Bazzi, H.; Lambert, J.-F. Formation of Activated Biomolecules by Condensation on Mineral Surfaces − A Comparison of Peptide Bond Formation and Phosphate Condensation. *Orig. Life Evol. Biosph.* **2013**, *43* (4), 429−443.

(28) Mohapatra, M.; Anand, S. Synthesis and applications of nano-structured iron oxides/hydroxides − a review. *Int. J. Eng. Sci. Tech.* **2011**, *2*, 8, .

(29) Kwon, K. D.; Kubicki, J. D. Molecular Orbital Theory Study on Surface Complex Structures of Phosphates to Iron Hydroxides: Calculation of Vibrational Frequencies and Adsorption Energies. *Langmuir* **2004**, *20* (21), 9249−9254.

(30) Kubicki, J. D.; Paul, K. W.; Kabalan, L.; Zhu, Q.; Mrozik, M. K.; Aryanpour, M.; Pierre-Louis, A.-M.; Strongin, D. R. ATR−FTIR and Density Functional Theory Study of the Structures, Energetics, and Vibrational Spectra of Phosphate Adsorbed onto Goethite. *Langmuir* **2012**, *28* (41), 14573−14587.

(31) Ganta, P. B.; Morshedizad, M.; Kühn, O.; Leinweber, P.; Ahmed, A. A. The Binding of Phosphorus Species at Goethite: A Joint Experimental and Theoretical Study. *Minerals* **2021**, *11* (3), 323.

(32) Liu, J.; Zhu, R.; Ma, L.; Fu, H.; Lin, X.; Parker, S. C.; Molinari, M. Adsorption of Phosphate and Cadmium on Iron (Oxyhydr)-Oxides: A Comparative Study on Ferrihydrite, Goethite, and Hematite. *Geoderma* **2021**, *383*, 114799.

(33) Kim, J.; Li, W.; Philips, B. L.; Grey, C. P. Phosphate Adsorption on the Iron Oxyhydroxides Goethite (α-FeOOH), Akaganeite (β-FeOOH), and Lepidocrocite (γ-FeOOH): A 31P NMR Study. *Energy Environ. Sci.* **2011**, *4* (10), 4298−4305.

(34) Mäkie, P.; Persson, P.; Österlund, L. Adsorption of Trimethyl Phosphate and Triethyl Phosphate on Dry and Water Pre-Covered Hematite, Maghemite, and Goethite Nanoparticles. *J. Colloid Interface Sci.* **2013**, *392*, 349−358.

(35) Zhang, L.; Gao, Y.; Xu, Y.; Liu, J. Different Performances and Mechanisms of Phosphate Adsorption onto Metal Oxides and Metal Hydroxides: A Comparative Study. *J. Chem. Technol. Biotechnol.* **2016**, *91* (5), 1232−1239.

(36) Feng, H.; Ma, S.; Chen, Z.; Li, Y.; Wang, M.; Ding, Y. Adsorption of Nucleotides and Nucleic Acids on Goethite Nanoparticles: Mode, Sites and Relationship with Phosphate and Non-Phosphate Structures. *Environ. Sci.: Nano* **2024**, *11*, 2655.

(37) Schmidt, M. P.; Martínez, C. E. Ironing Out Genes in the Environment: An Experimental Study of the DNA−Goethite Interface. *Langmuir* **2017**, *33* (34), 8525−8532.

(38) Barrón, V.; Torrent, J. Surface Hydroxyl Configuration of Various Crystal Faces of Hematite and Goethite. *J. Colloid Interface Sci* **1996**, *177* (2), 407−410.

https://doi.org/10.1021/acs.est.4c12049
Environ. Sci. Technol. 2025, 59, 5568−5584

(39) Song, X.; Boily, J.-F. Structural Controls on OH Site Availability and Reactivity at Iron Oxyhydroxide Particle Surfaces. *Phys. Chem. Chem. Phys.* **2012**, *14* (8), 2579−2586.
(40) Boily, J.-F.; Song, X. Direct Identification of Reaction Sites on Ferrihydrite. *Commun. Chem.* **2020**, *3* (1), 1−8.
(41) Ding, X.; Song, X.; Boily, J.-F. Identification of Fluoride and Phosphate Binding Sites at FeOOH Surfaces. *J. Phys. Chem. C* **2012**, *116* (41), 21939−21947.
(42) Elzinga, E.; Sparks, D. L. Phosphate Adsorption onto Hematite: An in Situ ATR-FTIR Investigation of the Effects of pH and Loading Level on the Mode of Phosphate Surface Complexation. *J. Colloid Interface Sci.* **2007**, *308* (1), 53−70.
(43) Turner, B. L.; Mahieu, N.; Condron, L. M. Phosphorus-31 Nuclear Magnetic Resonance Spectral Assignments of Phosphorus Compounds in Soil NaOH−EDTA Extracts. *Soil Sci. Soc. Am. J.* **2003**, *67* (2), 497−510.
(44) Metcalf, W. W.; van der Donk, W. A. Biosynthesis of Phosphonic and Phosphinic Acid Natural Products. *Annu. Rev. Biochem.* **2009**, *78*, 65−94.
(45) Newman, R. H.; Tate, K. R. Soil Phosphorus Characterisation by 31p Nuclear Magnetic Resonance. *Commun. Soil Sci. Plant Anal.* **1980**, *11* (9), 835−842.
(46) Sannigrahi, P.; Ingall, E. D.; Benner, B. Nature and Dynamics of Phosphorus-Containing Components of Marine Dissolved and Particulate Organic Matter. *Geochim. Cosmochim. Acta* **2006**, *70* (23), 5868−5882.
(47) Zhang, K.; Ho, K.-P.; Chatterjee, A.; Park, G.; Li, Z.; Catalano, J. G.; Parker, K. M. RNA Hydrolysis at Mineral−Water Interfaces. *Environ. Sci. Technol.* **2023**, *57* (22), 8280−8288.
(48) Schwertmann, U.; Cornell, R. M. Iron Oxides in the Laboratory. *Prep. Charact.* **1991**, .
(49) Lipps, W.; Baxter, T.; Braun-Howland, E. *Standard Methods For the Examination of Water and Wastewater*, 20 th ed.; APHA Press: Washington DC, 1998.
(50) Ravel, B.; Newville, M. ATHENA, ARTEMIS, HEPHAESTUS: Data Analysis for X-Ray Absorption Spectroscopy Using IFEFFIT. *J. Synchrotron Rad.* **2005**, *12* (4), 537−541.
(51) BIOVIA *Materials Studio*; Dassault Systemes, 2024.
(52) Yang, H.; Lu, R.; Downs, R. T.; Costin, G. Goethite, α-FeO(OH), from Single-Crystal Data. *Acta Cryst. E* **2006**, *62* (12), i250−i252.
(53) Blake, R. L.; Hessevick, R. E.; Zoltai, T.; Finger, L. W. Refinement of the Hematite Structure. *Am. Mineral*, **1966**, *51*, 1−2, pp. 123−129.
(54) Manceau, A.; Skanthakumar, S.; Soderholm, L. PDF Analysis of Ferrihydrite: Critical Assessment of the under-Constrained Akdalaite Model. *Am. Mineral* **2014**, *99* (1), 102−108.
(55) Sassi, M.; Chaka, A. M.; Rosso, K. M. Ab Initio Thermodynamics Reveals the Nanocomposite Structure of Ferrihydrite. *Commun. Chem.* **2021**, *4* (1), 1−10.
(56) Cygan, R. T.; Liang, J.-J.; Kalinichev, A. G. Molecular Models of Hydroxide, Oxyhydroxide, and Clay Phases and the Development of a General Force Field. *J. Phys. Chem. B* **2004**, *108* (4), 1255−1266.
(57) Ribeiro, A. J. M.; Ramos, M. J.; Fernandes, P. A. Benchmarking of DFT Functionals for the Hydrolysis of Phosphodiester Bonds. *J. Chem. Theory Comput.* **2010**, *6* (8), 2281−2292.
(58) Hirshfeld, F. L. Bonded-Atom Fragments for Describing Molecular Charge Densities. *Theoret. Chim. Acta* **1977**, *44* (2), 129−138.
(59) Mark, P.; Nilsson, L. Structure and Dynamics of the TIP3P, SPC, and SPC/E Water Models at 298 K. *J. Phys. Chem. A* **2001**, *105* (43), 9954−9960.
(60) Akkermans, R. L. C.; Spenley, N. A.; Robertson, S. H. COMPASS III: Automated Fitting Workflows and Extension to Ionic Liquids. *Mol. Simul.* **2021**, *47* (7), 540−551.
(61) Kennard, O.; Isaacs, N. W.; Motherwell, W. D. S.; Coppola, J. C.; Wampler, D. L.; Larson, A. C.; Watson, D. G.; Todd, A. R. The Crystal and Molecular Structure of Adenosine Triphosphate. *Proc. R. Soc. London, A* **1971**, *325* (1562), 401−436.
(62) Larson, A. C. Restrained Refinement of Disodium Adenosine 5′-Triphosphate Trihydrate. *Acta Crystallogr., Sect. B* **1978**, *34* (12), 3601−3604.
(63) Bhushan, B.; Shanker, U.; Kamaluddin. Adsorption of Ribose Nucleotides on Manganese Oxides with Varied Mn/O Ratio: Implications for Chemical Evolution. *Orig. Life Evol. Biosph.* **2011**, *41* (5), 469−482.
(64) Wan, B.; Huang, R.; Diaz, J. M.; Tang, Y. Polyphosphate Adsorption and Hydrolysis on Aluminum Oxides. *Environ. Sci. Technol.* **2019**, *53* (16), 9542−9552.
(65) Tajmir-Riahi, H. A.; Bertrand, M. J.; Theophanides, T. Synthesis, Structure, Proton-Nuclear Magnetic Resonance, and Fourier Transform Infrared Spectroscopy of Several Transition and Nontransition Metal−Adenosine-5-Triphosphate Complexes. *Can. J. Chem.* **1986**, *64* (5), 960−966.
(66) Tajmir-Riahi, H. A.; Theophanides, T. Adenosine-5′-Monophosphate Complexes of Pt(II) and Mg(II) Metal Ions. Synthesis, FT IR Spectra and Structural Studies. *Inorg. Chim. Acta* **1983**, *80*, 183−190.
(67) Banyay, M.; Sarkar, M.; Gräslund, A. A Library of IR Bands of Nucleic Acids in Solution. *Biophys. Chem.* **2003**, *104* (2), 477−488.
(68) Arai, Y.; Sparks, D. L. ATR−FTIR Spectroscopic Investigation on Phosphate Adsorption Mechanisms at the Ferrihydrite−Water Interface. *J. Colloid Interface Sci.* **2001**, *241* (2), 317−326.
(69) Ahmed, A. A.; Gypser, S.; Leinweber, P.; Freese, D.; Kühn, O. Infrared Spectroscopic Characterization of Phosphate Binding at the Goethite−Water Interface. *Phys. Chem. Chem. Phys.* **2019**, *21* (8), 4421−4434.
(70) Fang, Y.; Kim, E.; Strathmann, T. J. Mineral- and Base-Catalyzed Hydrolysis of Organophosphate Flame Retardants: Potential Major Fate-Controlling Sink in Soil and Aquatic Environments. *Environ. Sci. Technol.* **2018**, *52* (4), 1997−2006.
(71) Torrents, A.; Stone, A. T. Hydrolysis of Phenyl Picolinate at the Mineral/Water Interface. *Environ. Sci. Technol.* **1991**, *25* (1), 143−149.
(72) Müller, W. E. G.; Schröder, H. C.; Wang, X. The Phosphoanhydride Bond: One Cornerstone of Life. *Biochemist* **2019**, *41* (4), 22−27.
(73) Margalef, O.; Sardans, J.; Fernández-Martínez, M.; Molowny-Horas, R.; Janssens, I. A.; Ciais, P.; Goll, D.; Richter, A.; Obersteiner, M.; Asensio, D.; Peñuelas, J. Global Patterns of Phosphatase Activity in Natural Soils. *Sci. Rep.* **2017**, *7* (1), 1337.
(74) Huang, Q.; Zhao, Z.; Chen, W. Effects of Several Low-Molecular Weight Organic Acids and Phosphate on the Adsorption of Acid Phosphatase by Soil Colloids and Minerals. *Chemosphere* **2003**, *52* (3), 571−579.
(75) Tietjen, T.; Wetzel, R. G. Extracellular Enzyme-Clay Mineral Complexes: Enzyme Adsorption, Alteration of Enzyme Activity, and Protection from Photodegradation. *Aquat. Ecol.* **2003**, *37* (4), 331−339.
(76) Wang, J.; Bai, Z. Fe-Based Catalysts for Heterogeneous Catalytic Ozonation of Emerging Contaminants in Water and Wastewater. *Chem. Eng. J.* **2017**, *312*, 79−98.
(77) Chen, L.; Wang, H.; Sun, Y.; Zhao, Y.; Shi, H. Interface Mechanisms of the Catalytic Ozonation of Humic Acids over Siliceous Ferrihydrite: Morphology, Stability, and the Catalytic Process. *Environ. Res.* **2022**, *203*, 111870.
(78) McLaren, T. I.; Smernik, R. J.; McLaughlin, M. J.; McBeath, T. M.; Kirby, J. K.; Simpson, R. J.; Guppy, C. N.; Doolette, A. L.; Richardson, A. E. Complex Forms of Soil Organic Phosphorus−A Major Component of Soil Phosphorus. *Environ. Sci. Technol.* **2015**, *49* (22), 13238−13245.
(79) Vincent, A. G.; Vestergren, J.; Gröbner, G.; Persson, P.; Schleucher, J.; Giesler, R. Soil Organic Phosphorus Transformations in a Boreal Forest Chronosequence. *Plant Soil* **2013**, *367* (1), 149−162.
(80) Dannenberg, A.; Pehkonen, S. O. Investigation of the Heterogeneously Catalyzed Hydrolysis of Organophosphorus Pesticides. *J. Agric. Food Chem.* **1998**, *46* (1), 325−334.

https://doi.org/10.1021/acs.est.4c12049
Environ. Sci. Technol. 2025, 59, 5568−5584

(81) Sulieman, S.; Mühling, K. H. Utilization of Soil Organic Phosphorus as a Strategic Approach for Sustainable Agriculture. *J. Plant Nutr. Soil Sci.* **2021**, *184* (3), 311−319.
(82) Roberts, T. L.; Johnston, A. E. Phosphorus Use Efficiency and Management in Agriculture. *Res. Conserv. Recyc.* **2015**, *105*, 275−281.
(83) Stutter, M. I.; Shand, C. A.; George, T. S.; Blackwell, M. S. A.; Bol, R.; MacKay, R. L.; Richardson, A. E.; Condron, L. M.; Turner, B. L.; Haygarth, P. M. Recovering Phosphorus from Soil: A Root Solution? *Environ. Sci. Technol.* **2012**, *46* (4), 1977−1978.
(84) Cade-Menun, B. J. Characterizing Phosphorus Forms in Cropland Soils with Solution 31P-NMR: Past Studies and Future Research Needs. *Chem. Biol. Technol. Agric.* **2017**, *4* (1), 1−12.
(85) George, T. S.; Giles, C. D.; Menezes-Blackburn, D.; Condron, L. M.; Gama-Rodrigues, A. C.; Jaisi, D.; Lang, F.; Neal, A. L.; Stutter, M. I.; Almeida, D. S.; Bol, R.; Cabugao, K. G.; Celi, L.; Cotner, J. B.; Feng, G.; Goll, D. S.; Hallama, M.; Krueger, J.; Plassard, C.; Rosling, A.; Darch, T.; Fraser, T.; Giesler, R.; Richardson, A. E.; Tamburini, F.; Shand, C. A.; Lumsdon, D. G.; Zhang, H.; Blackwell, M. S. A.; Wearing, C.; Mezeli, M. M.; Almås, Å. R.; Audette, Y.; Bertrand, I.; Beyhaut, E.; Boitt, G.; Bradshaw, N.; Brearley, C. A.; Bruulsema, T. W.; Ciais, P.; Cozzolino, V.; Duran, P. C.; Mora, M. L.; de Menezes, A. B.; Dodd, R. J.; Dunfield, K.; Engl, C.; Frazão, J. J.; Garland, G.; González Jiménez, J. L.; Graca, J.; Granger, S. J.; Harrison, A. F.; Heuck, C.; Hou, E. Q.; Johnes, P. J.; Kaiser, K.; Kjær, H. A.; Klumpp, E.; Lamb, A. L.; Macintosh, K. A.; Mackay, E. B.; McGrath, J.; McIntyre, C.; McLaren, T.; Mészáros, E.; Missong, A.; Mooshammer, M.; Negrón, C. P.; Nelson, L. A.; Pfahler, V.; Poblete-Grant, P.; Randall, M.; Seguel, A.; Seth, K.; Smith, A. C.; Smits, M. M.; Sobarzo, J. A.; Spohn, M.; Tawaraya, K.; Tibbett, M.; Voroney, P.; Wallander, H.; Wang, L.; Wasaki, J.; Haygarth, P. M. Organic Phosphorus in the Terrestrial Environment: A Perspective on the State of the Art and Future Priorities. *Plant Soil* **2018**, *427* (1), 191−208.
(86) Turner, B. L.; Papházy, M. J.; Haygarth, P. M.; McKelvie, I. D. Inositol Phosphates in the Environment. *Philos. Trans R Soc. Lond B Biol. Sci.* **2002**, *357* (1420), 449−469.
(87) Solhtalab, M.; Moller, S. R.; Gu, A. Z.; Jaisi, D.; Aristilde, L. Selectivity in Enzymatic Phosphorus Recycling from Biopolymers: Isotope Effect, Reactivity Kinetics, and Molecular Docking with Fungal and Plant Phosphatases. *Environ. Sci. Technol.* **2022**, *56* (22), 16441−16452.
(88) Guo, M.; Li, X.; Wang, Y.; Zhang, Y.; Fu, Q.; Huguet, A.; Liu, G. New Insights into the Mechanism of Phosphate Release during Particulate Organic Matter Photodegradation Based on Optical and Molecular Signatures. *Water Res.* **2023**, *236*, 119954.
(89) Southwell, M. W.; Kieber, R. J.; Mead, R. N.; Brooks Avery, G.; Skrabal, S. A. Effects of Sunlight on the Production of Dissolved Organic and Inorganic Nutrients from Resuspended Sediments. *Biogeochemistry* **2010**, *98* (1), 115−126.
(90) Shand, C. A.; Cheshire, M. V.; Bedrock, C. N.; Chapman, P. J.; Fraser, A. R.; Chudek, J. A. Solid-Phase 31P NMR Spectra of Peat and Mineral Soils, Humic Acids and Soil Solution Components: Influence of Iron and Manganese. *Plant Soil* **1999**, *214* (1), 153−163.
(91) Post, J. E. Manganese Oxide Minerals: Crystal Structures and Economic and Environmental Significance. *Proc. Natl. Acad. Sci. U. S. A.* **1999**, *96* (7), 3447−3454.
(92) Schroth, A. W.; Giles, C. D.; Isles, P. D. F.; Xu, Y.; Perzan, Z.; Druschel, G. K. Dynamic Coupling of Iron, Manganese, and Phosphorus Behavior in Water and Sediment of Shallow Ice-Covered Eutrophic Lakes. *Environ. Sci. Technol.* **2015**, *49* (16), 9758−9767.
(93) Li, H.; Santos, F.; Butler, K.; Herndon, E. A Critical Review on the Multiple Roles of Manganese in Stabilizing and Destabilizing Soil Organic Matter. *Environ. Sci. Technol.* **2021**, *55* (18), 12136−12152.
(94) Reardon, P. N.; Chacon, S. S.; Walter, E. D.; Bowden, M. E.; Washton, N. M.; Kleber, M. Abiotic Protein Fragmentation by Manganese Oxide: Implications for a Mechanism to Supply Soil Biota with Oligopeptides. *Environ. Sci. Technol.* **2016**, *50* (7), 3486−3493.
(95) Weng, L.; Van Riemsdijk, W. H.; Hiemstra, T. Humic Nanoparticles at the Oxide−Water Interface: Interactions with Phosphate Ion Adsorption. *Environ. Sci. Technol* **2008**, *42* (23), 8747−8752.
(96) Ohno, T.; Kubicki, J. D. Adsorption of Organic Acids and Phosphate to an Iron (Oxyhydr)Oxide Mineral: A Combined Experimental and Density Functional Theory Study. *J. Phys. Chem. A* **2020**, *124* (16), 3249−3260.
(97) Lindegren, M.; Persson, P. Competitive Adsorption between Phosphate and Carboxylic Acids: Quantitative Effects and Molecular Mechanisms. *Eur. J. Soil Sci.* **2009**, *60* (6), 982−993.

https://doi.org/10.1021/acs.est.4c12049
Environ. Sci. Technol. 2025, 59, 5568−5584